

## Investigating the Mechanisms of an Intense Coastal Rainfall Event during TAHOPE/PRECIP-IOP3 Using a Multiscale Radar Ensemble Data Assimilation System

SHU-CHIH YANG,<sup>a</sup> SHU-HUA CHEN<sup>✉,b</sup> LAWRENCE JING-YUEH LIU,<sup>a</sup> HAO-LUN YEH,<sup>a</sup> WEI-YU CHANG,<sup>a</sup> KAO-SHEN CHUNG,<sup>a</sup> PAO-LIANG CHANG,<sup>c</sup> AND WEN-CHAU LEE<sup>d</sup>

<sup>a</sup> Department of Atmospheric Sciences, National Central University, Taoyuan, Taiwan

<sup>b</sup> Department of Land, Air and Water Resources, University of California, Davis, Davis, California

<sup>c</sup> Central Weather Administration, Taipei, Taiwan

<sup>d</sup> Earth Observing Laboratory, NCAR, Boulder, Colorado

(Manuscript received 14 March 2024, in final form 12 September 2024, accepted 16 September 2024)

**ABSTRACT:** The joint Taiwan-Area Heavy Rain Observation and Prediction Experiment (TAHOPE)/Prediction of Rainfall Extremes Campaign in the Pacific (PRECIP) field campaign between Taiwan and the United States took place from late May to mid-August in 2022. The field campaign aimed to understand the dynamics, thermodynamics, and predictability of heavy rainfall events in the Taiwan area. This study investigated the mechanisms of a heavy rainfall event that occurred on 6–7 June during the intensive observation period 3 (IOP3) of the field campaign. Heavy rainfall occurs on Taiwan's western coast when a mei-yu front hovers in northern Taiwan. A multiscale radar ensemble data assimilation system based on the successive covariance localization (SCL) method is used to derive a high-resolution analysis for forecasts. Two numerical experiments are conducted with the use of convective-scale (Experiment RDA) or multiscale (Experiment MRDA) corrections in the assimilation of the radial velocity from operational radars at Chigu and WuFen and the additional S-band dual-polarization Doppler radar (S-Pol) deployed at Hsinchu during the field campaign. Compared with RDA, MRDA results in large-area wind corrections, which help reshape and relocate a low-level mesoscale vortex, a key element of this heavy rainfall event, offshore of western central Taiwan and enhances the front intensity offshore of northwestern Taiwan. Consequently, MRDA improves the 6-h heavy rainfall prediction over the coast of western Taiwan and better represents the elongated rainband in northern Taiwan during the 3–6-h forecast. Sensitivity experiments demonstrate the importance of assimilating winds from Chigu and S-Pol radar in establishing low-level mesoscale vortex and convergence zones.

**KEYWORDS:** Convective storms; Mei-yu fronts; Nowcasting; Numerical weather prediction/forecasting; Data assimilation

### 1. Introduction

Severe weather systems commonly involve multiscale features, such as monsoons, frontal systems, and tropical cyclones (TCs), whose influence on human lives and economies can range from very local (e.g., severe convective cells in a frontal system) to broad (e.g., TCs).

The mei-yu front, which is called the baiu front in Japan and the changma front in Korea, is a stationary front and a major multiscale weather phenomenon in East Asia that occurs from the middle of May to the end of June. While the mei-yu front plays a critical role in supplying water to many countries in the area, it can also produce extreme rainfall, causing major floods and mudslides (Lin and Chen 2012). The duration, orientation, location, and intensity of mei-yu or mei-yu-related rainfall events are sensitive to the interplay of the characteristics of weather phenomena at different scales, such as synoptic-scale southwesterly monsoonal flow, mesoscale weather systems, front intensity, and convective cells. Southwesterly flow plays a critical role in moisture transport

and is thus deterministic for rainfall intensity (Chen et al. 2005; Tu et al. 2022). The rainfall duration can be lengthened with the occurrence of mesoscale convective systems (MCSs) in the prefrontal zone or blocking via a midlatitude omega anticyclone (Luo and Chen 2015; Hsiao and Chen 2014).

In Taiwan, the mei-yu-related rainfall can be redistributed and enhanced by orographic lifting due to its complex high mountains (Fig. 1a). In addition, the orographic blocking effect can induce the barrier jet to enhance convergence off the coast, generating intense deep convection (Chen et al. 2018; Ke et al. 2019) and slowing the progression of the southward-moving front in northern Taiwan (Tu et al. 2022). As a result, even under similar large-scale conditions (e.g., moist southwesterly flow) but with small variations, the mei-yu rainfall intensity and distribution can vary substantially, thereby lowering their predictability.

The importance, complex multiscale interactions, and low predictability of the mei-yu front and its related heavy rainfall have made this weather phenomenon a target in different field campaigns in East Asia, such as Southwestern Monsoon Experiment (SoWMEX)/Terrain-influenced Monsoon Rainfall Experiment (TiMRex) (Jou et al. 2011) and Taiwan Area Mesoscale Experiment (TAMEX) (Kuo and Chen 1990). Most recently, the joint Taiwan-Area Heavy Rain Observation and Prediction Experiment (TAHOPE)/Prediction of Rainfall Extremes Campaign in the Pacific (PRECIP) field

<sup>✉</sup> Denotes content that is immediately available upon publication as open access.

Corresponding author: Shu-Hua Chen, shachen@ucdavis.edu

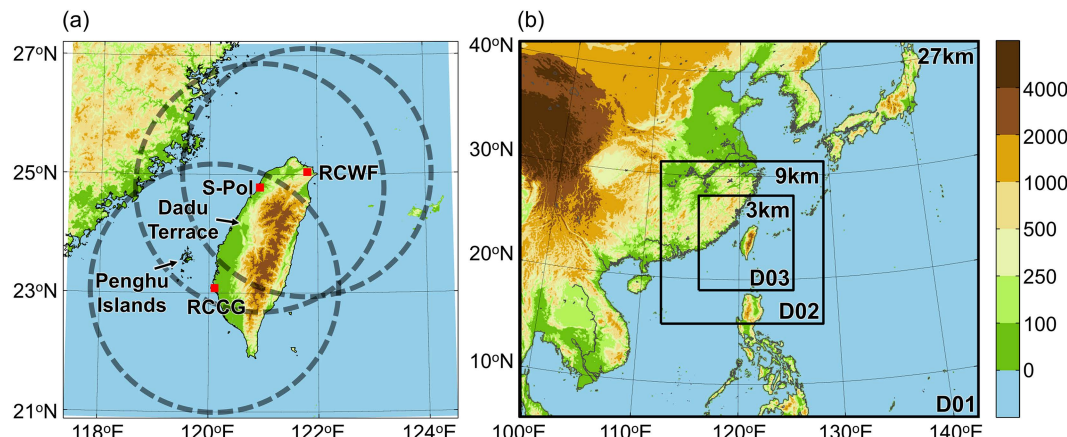


FIG. 1. (a) Topography of Taiwan and the locations of three radars (RCCG, RCWF, and S-Pol) and their observing ranges (dashed circles). (b) The three nested domains and their horizontal resolutions used in the analysis cycles and forecasts.

campaign between Taiwan and the United States was conducted from late May to mid-August in 2022; in the joint field campaign, data were collected, particularly from radars and radiosondes, for heavy rainfall events across the spectrum of different precipitation intensities and durations from the mei-yu season to the middle of the tropical cyclone season (Zhang et al. 2023). With field data, TAHOPE/PRECIP aims to understand the dynamics, thermodynamics, and predictability of heavy rainfall events in northern Taiwan.

This study was motivated by the poor heavy rainfall forecast associated with a mei-yu front system and the disagreement in rainfall forecasts among different models for 6–7 June 2022 over the western coast of Taiwan during intensive observation period 3 (IOP3) in the TAHOPE/PRECIP (details to be discussed in section 2). The low predictability of the heavy rainfall event could be attributed to uncertainties in different scales of weather systems and the interactions of these weather systems with complex terrain. This was the motivation for deploying the S-band dual-polarization Doppler radar (S-Pol) in Hsinchu to capture the structure of the southward-moving mei-yu front and convective systems over the northwestern Taiwan region when designing the field campaign. Therefore, it is scientifically interesting to ask, “Can the heavy rainfall forecast be improved by using additional S-Pol radar data from the field campaign?” “Will different assimilation strategies change the outcome of the forecast?” The answers to these questions can be achieved through the application of rapid-update convective-scale assimilation, which allows the correction of small-scale characteristics in the model state. Unlike previous field campaigns, the application of data assimilation techniques and strategies is one of TAHOPE/PRECIP’s emphases since high-resolution four-dimensional gridded data can be used to study the evolution of heavy rainfall events.

Conventionally, very short-term precipitation prediction is initialized from high-resolution analysis derived from convective-scale data assimilation with frequent analysis cycles and a short assimilation period in a limited area. During rapid

update cycles, convective-scale corrections are derived without updating the synoptic and mesoscale components. Given the multiscale characteristics of the heavy rainfall event of interest, multiscale analysis corrections should be incorporated to obtain accurate initial conditions for the forecast. Following this concept, blending global analysis with convective-scale analysis is a common strategy that is operationally adopted. However, global analysis constrains large-scale features without feedback from small-scale corrections. Additionally, the inconsistency between the global- and convective-scale analyses derived from different analysis systems can introduce model shock to small-scale simulations at each blending. An optimal solution is to perform multiscale assimilation at the same analysis time using the same data assimilation system to allow for multiscale interactions during the analysis cycles.

Multiscale data assimilation with ensemble Kalman filter (EnKF) algorithms is achieved through two main types of implementations. The first type applies scale-dependent localization to the full-resolution ensemble-based background error covariance and derives multiscale analysis corrections simultaneously with a single step (Wang et al. 2021). The second type computes the analysis increments (corrections) at different scales separately with multiple analysis steps, such as successive covariance localization (SCL; Zhang et al. 2009) and the dual localization method (Miyoshi and Kondo 2013; Yang et al. 2017). The SCL method derives multiscale analysis corrections separately by assimilating observations that have been divided into different horizontal spatial densities with different localization scales. With localization flexibility for different variables, the SCL method has been adopted in the Weather Research and Forecasting (WRF) Model (Skamarock et al. 2019) coupled with the local ensemble transform Kalman filter (LETKF; Hunt et al. 2007) radar assimilation system (WLRAS; Tsai et al. 2014) to obtain multiscale analysis increments (Lin et al. 2022; Liu 2022).

This study applies the WLRAS-SCL framework to investigate the improvement in the forecast and associated mechanisms responsible for the multiscale heavy rainfall event on

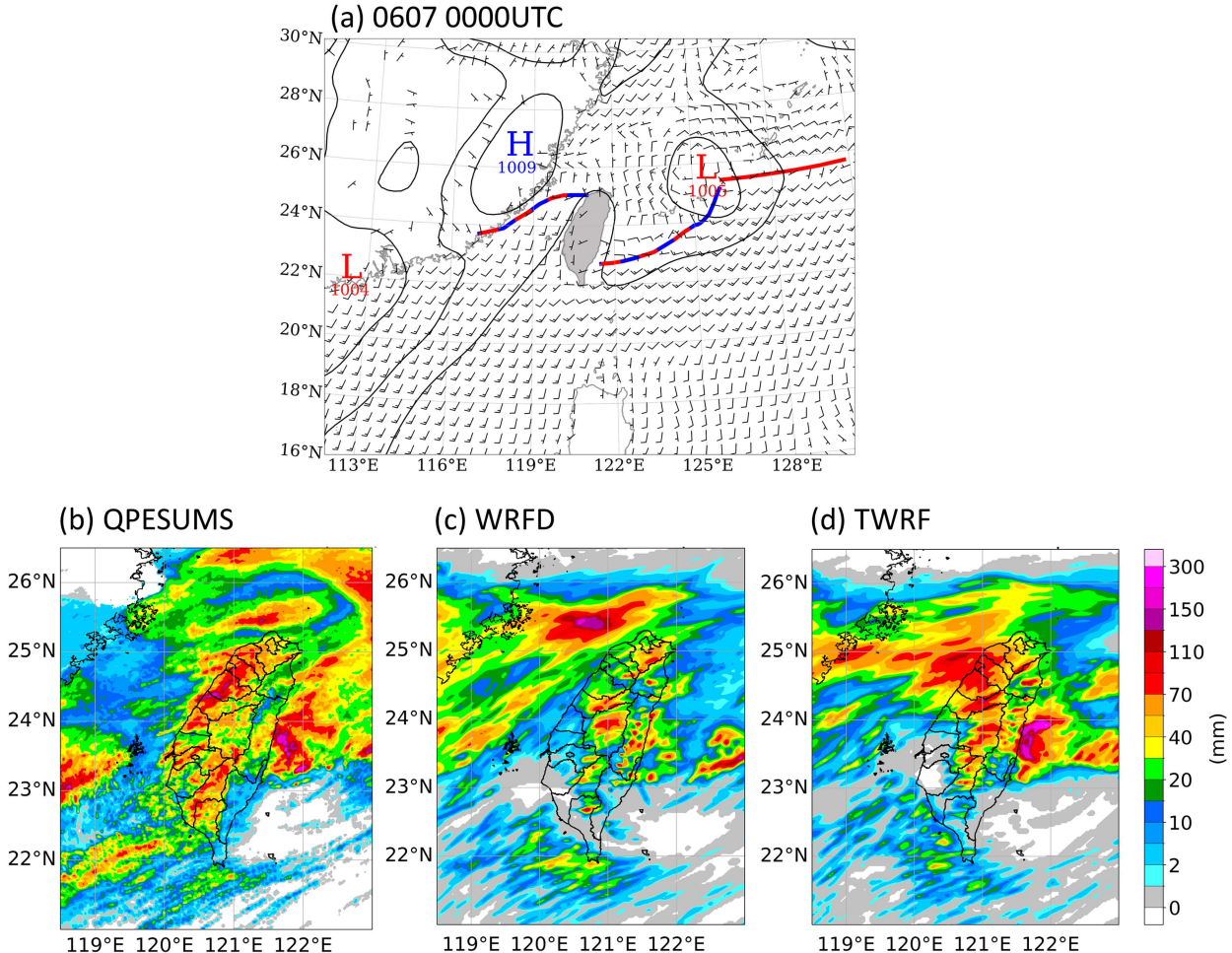


FIG. 2. (a) Synoptic-scale weather systems, 10-m wind barbs, and fronts at 0000 UTC 7 Jun 2022 plotted using the ECMWF ERA5. The stationary front symbol indicates the location of the mei-yu front, which extends to the east side of Taiwan. The black contours are sea level pressure with an interval of 1 hPa. The 12-h accumulated rainfall (mm) from 0000 to 1200 UTC 7 Jun from (b) the QPESUMS and two official Taiwan CWA operational (c) WRFD and (d) TWRFT forecasts. WRFD is a WRF configuration designed for regular deterministic weather forecasts, whereas TWRFT is a WRF configuration designed for typhoon forecasts at the CWA.

6–7 June 2022 in Taiwan during the TAHOPE/PRECIP IOP3. Traditionally, radar data are assimilated with convective-scale localization, and the impact is most critical during the first 3-h forecast. With multiscale corrections that range from those at small scales to those of environmental flow, the benefit of assimilating radar data can extend to several hours, which can potentially further improve the prediction of long-duration heavy rainfall events. In this study, we specifically aim to answer the following questions for the TAHOPE/PRECIP IOP3 rainfall event. Does the WLRAS-SCL framework add additional value to radar data assimilation for traditional convective-scale analysis and heavy rainfall prediction? What are the mechanisms that initialize and rapidly intensify coastal convection in western Taiwan? What is the role of offshore environmental flow in terms of dynamic and thermodynamic conditions?

The rest of the paper is organized as follows. Section 2 briefly overviews the TAHOPE/PRECIP IOP3 event. Section 3 introduces

the WLRAS-SCL framework, the radar data used in this study, and the numerical experimental design. Section 4 discusses the analysis and forecast results and explains the mechanisms responsible for the heavy rainfall over the western coast of Taiwan. Section 5 presents sensitivity experiment results to justify our arguments. Section 6 provides a quantitative evaluation of forecast skills. Finally, section 7 provides a brief summary and conclusions of this work.

## 2. Overview of the heavy rainfall event during TAHOPE/PRECIP IOP3

The TAHOPE/PRECIP IOP3 started at 0600 UTC 6 June. The mei-yu front of interest in the study was positioned offshore of northern Taiwan at this time. The front moved southward slowly and arrived in northern Taiwan 6 h later. Afterward, the front remained quasi-stationary between central and northern Taiwan, as shown at 0000 UTC 7 June as an example (Fig. 2a),

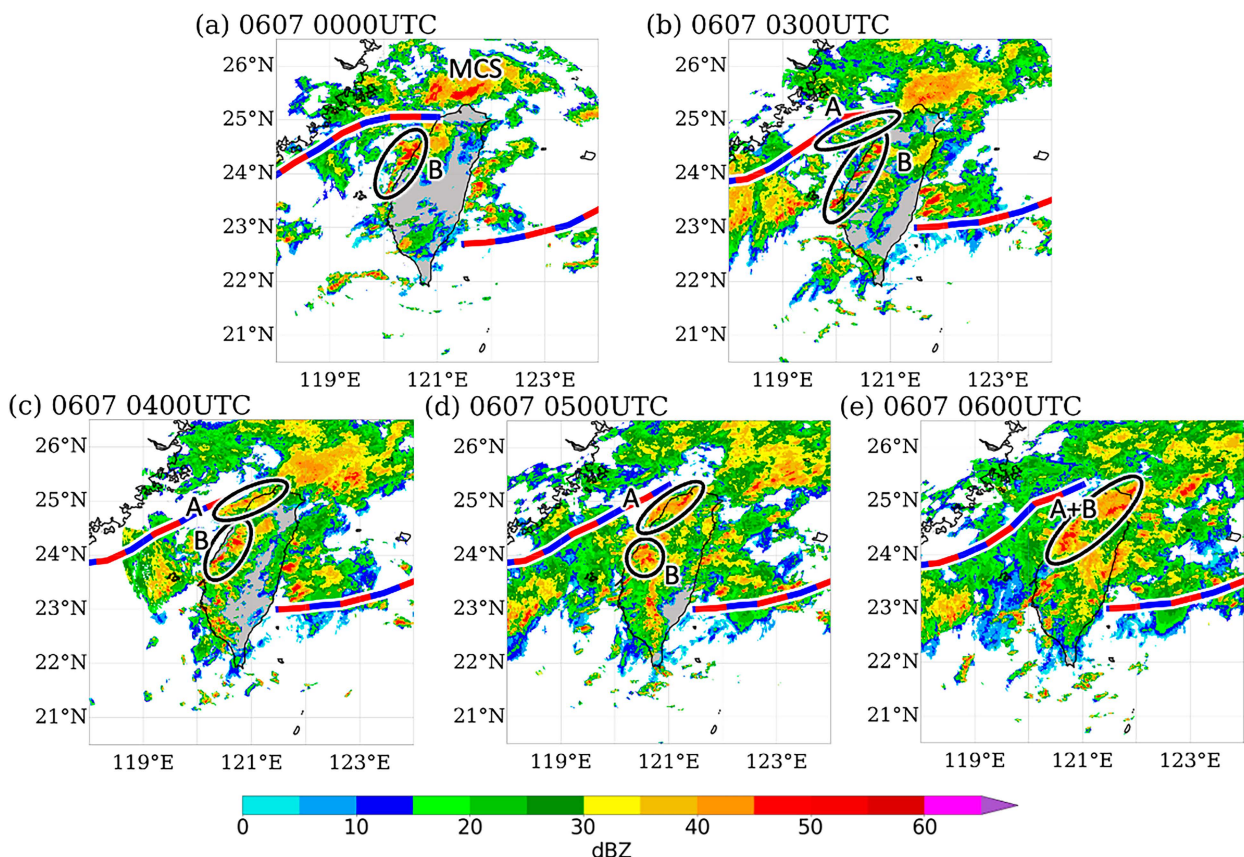


FIG. 3. The QPESUMS radar reflectivity at (a) 0000 UTC, (b) 0300 UTC, (c) 0400 UTC, (d) 0500 UTC, and (e) 0600 UTC 7 Jun 2022. The stationary front symbol indicates the location of the mei-yu front, which is defined by the strong horizontal potential temperature gradient near the surface using ERA5 data. The circles highlight the convective cells' locations of areas A and B (see the text for details). “MCS” indicates the location of the MCS.

and occasionally moved north of Taiwan until the end of IOP3. The original plan was to end IOP3 at 0600 UTC 9 June 2022. However, owing to the persistent lingering of the mei-yu front in the northern Taiwan area (Figs. 2a and 3a), poor rainfall forecasts (Fig. 2b vs Figs. 2c,d), and great disagreement in the rainfall intensity and location forecasts among different models (see Fig. 2c vs Fig. 2d for an example), IOP3 was extended to 1200 UTC 12 June. While IOP3 lasted for approximately 6 days, the major rainfall along the western coast occurred during the first 3 days, with the maximum accumulated amount approaching 300 mm. On 6 June, the maximum rainfall rate reached  $\sim 90 \text{ mm h}^{-1}$  at the coast near  $24.6^\circ\text{N}$  and  $120.8^\circ\text{E}$  from 2000 to 2100 UTC. On 7 June, the heaviest rainfall occurred between 0000 (0800 LST) and 1200 UTC (2000 LST). During this period, an extreme rainfall advisory was issued at several locations from early to late afternoon, including those near the western coast of central Taiwan and northern Taiwan. Although southern and southwestern Taiwan also received a large amount of rainfall during these 3 days, our major interest is placed on the heavy rainfall period from 0300 UTC (1100 LST) to 0900 UTC (1900 LST) on 7 June for the region from central to northern Taiwan, which is the region of focus of the TAHOPE/PRECIP field campaign.

In addition to the convective rainband along the mei-yu front of interest (Fig. 3), a few other precipitation systems in the Taiwan area that occurred during IOP3 also contributed to the heavy rainfall event and caused the low predictability of precipitation at the coast. Over the northern coast, an MCS located north of Taiwan swept through and produced rainfall in this area (Fig. 3a). In addition to the MCS that largely traveled north of Taiwan, a convective band developed along the mei-yu front around 0300 UTC (area A in Fig. 3b) together with a series of convective cells that developed along the western coast of Taiwan (area B in Figs. 3a,b). The western end of the convective band along the front bent southeastward and appressed to the coast of northwestern Taiwan during early 7 June (Fig. 3d). Later, the bent portion of the convective band moved inland. By 0600 UTC, these areas of convection merged and grew upscale into a convective rainband (Fig. 3e) that resulted in heavy rainfall at Dadu Terrace (see Fig. 1a for the location) and over northwestern and northern Taiwan. We note that convective systems west and southwest of Taiwan also moved into southwestern Taiwan and merged during this period, causing heavy rainfall in southern Taiwan.

During 6–7 June, the surface wind pattern over the Taiwan Strait differed remarkably between the fifth major global

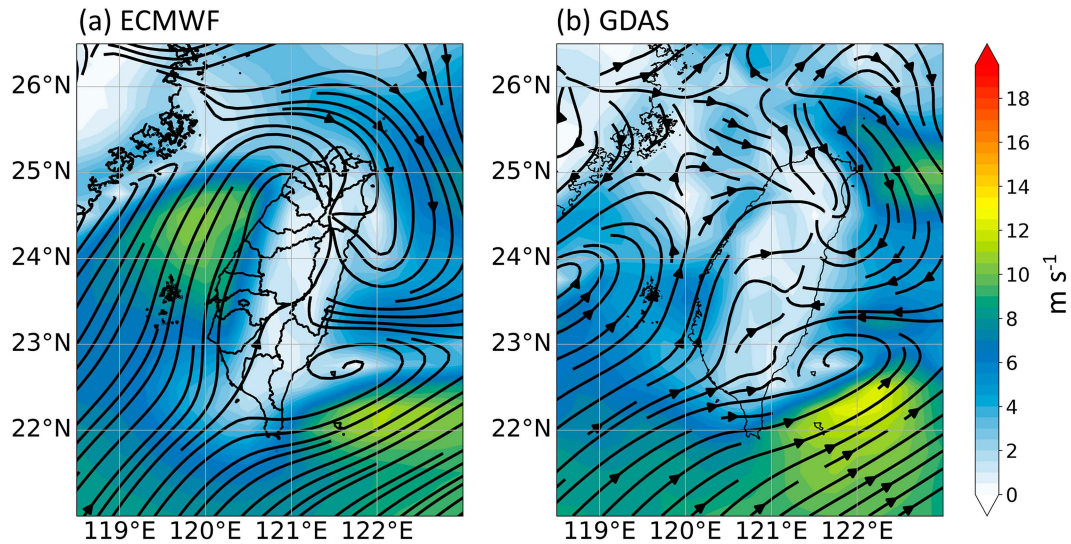


FIG. 4. The 975-hPa streamlines and 10-m wind speed ( $\text{m s}^{-1}$ ) from (a) ERA5 and (b) GDAS at 0000 UTC 7 Jun.

reanalysis produced by the European Centre for Medium-Range Weather Forecasts (ECMWF) (ERA5) and the National Centers for Environmental Prediction (NCEP) global final (FNL) analyses from the Global Data Assimilation System (GDAS). This echoes what was mentioned earlier concerning the large uncertainty in forecasted meso- to synoptic-scale features in this area for IOP3, as the real-time analysis (i.e., initial conditions) and forecasts produced by the ECMWF Integrated Forecasting System and NCEP Global Forecast System were used to drive mesoscale or global model forecasts during the field campaign. For example, unlike the ERA5 data, in which higher wind speeds appear west of central Taiwan (Fig. 4a), the wind speeds in the GDAS analysis were weaker (Fig. 4b). In addition, a mesoscale vortex appeared at  $\sim 23.5^\circ\text{N}$  and  $118^\circ\text{E}$  in the GDAS but was absent in ERA5. Although the operational regional forecasts showed some ability to predict the precipitation in the frontal zone, the location of heavy rainfall over the western coast was misforecasted (Figs. 2c,d vs Fig. 2b). Without having accurate dynamic and thermodynamic conditions offshore in the initial conditions, it is difficult to predict this rainfall event in the western coastal region. Thus, this study aims to investigate the mechanisms supporting the development of rapid convection on the western coast via radar data assimilation and forecasts.

### 3. Data assimilation system and numerical experimental design

#### a. WRF-LETKF radar assimilation system with successive covariance localization

The WRF-LETKF radar assimilation system (WLRAS; Tsai et al. 2014) is used to assimilate the radar data in this study. The WLRAS has been successfully applied to investigate the very short-term predictability of heavy rainfall events in Taiwan (Yang et al. 2022; Wu et al. 2020; Yeh et al. 2022;

Do et al. 2022). The WLRAS assimilates radar observations sequentially with high flexibility in applying different localizations to different variables. Recently, the SCL method has been implemented in the WLRAS to derive multiscale wind corrections with the assimilation of radial velocity (Lin et al. 2022; Liu 2022). Lin et al. (2022) confirmed that SCL substantially increased the observational impact by enhancing typhoon circulation at the mesoalpha scale and, consequently, improved the intensity forecast. Here, the WLRAS-SCL framework is adopted to investigate how the dynamic and thermodynamic conditions offshore of western Taiwan affect rapid convection development on the western coast.

Despite the fact that radar has a limitation in observing the near-surface conditions due to a nonzero elevation angle, the near-surface conditions can be modified through a separate larger-scale dynamic adjustment from assimilating the radial velocity close to the radar site (i.e., at low altitude) during the first iteration of the SCL algorithm. The larger-scale correction by SCL also allows us to investigate the role of environmental flow and long-range moisture transport from upstream.

#### b. Radar data

During the TAHOPE/PRECIP field campaign, additional instruments, including micropulse differential absorption lidar (DIAL) (MPD), radiosondes in Hsinchu, and radars [S-Pol radar and Taiwan Experimental Atmospheric Mobile-Radar (TEAM-R)], were deployed over northern Taiwan. Very little MPD data from the Hsinchu site were available during the study period. Although three radiosonde soundings were available within the area of interest at 0000 UTC 7 June, we chose not to assimilate MPD and radiosonde data since we wanted to exclusively examine the impact of multiscale corrections from assimilating dense radar data on heavy rainfall forecasts caused by convective cells.

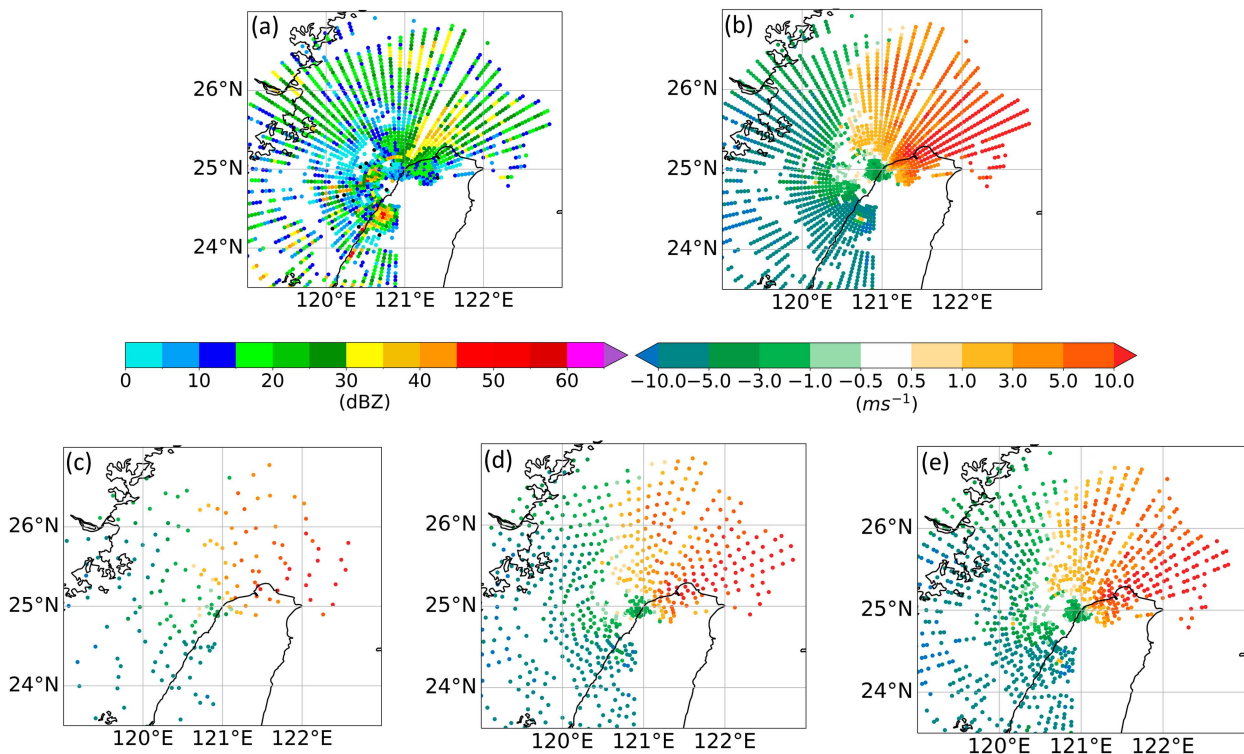


FIG. 5. Superobservations of (a) reflectivity and (b) radial velocity from the S-Pol radar at 0300 UTC 7 Jun. Subsets of the radial velocity obtained by taking (c) 10%, (d) 30%, and (e) 60% of the data in (b).

The radar data used in this study include the radial velocity ( $V_r$ ) and reflectivity ( $Z_h$ ) data obtained from the S-band Doppler radars at Wufenshan (RCWF), Chigu (RCCG), and Hsinchu (Fig. 1a). The first two radars are regular Central Weather Administration (CWA) radars in Taiwan. The third radar is the National Center for Atmospheric Research (NCAR) S-Pol radar from PRECIP. The spatial resolutions for the azimuthal angle and range gate are  $0.5^\circ \times 250$  m for RCWF,  $1^\circ \times 250$  m for RCCG, and  $0.75^\circ \times 150$  m for S-Pol. Notably, other CWA radars were available during the field campaign. However, since radar data quality is crucial to the assimilation results and data quality control (QC) requires significant effort in processing (see the appendix) and supervising, we chose to process and use data from these three radars for the study since they were at critical locations.

To ensure the quality of the radar datasets, a rigorous QC process was implemented using Taiwan's National Central University (NCU) Radar Laboratory's RAKIT (Radar kit) software (the appendix). Eliminating data points that are prone to spurious corrections in the wind and geopotential height fields is crucial during assimilation, particularly for multiscale corrections (Liu 2022). The QCed radar data were resampled to superobservations with a spatial resolution of  $5^\circ \times 5$  km in the azimuth  $\times$  range gate directions. This choice was made to reduce the representative error, which is consistent with previous studies (Yeh et al. 2022). The observational errors are set to 5 dBZ for the reflectivity and  $3 \text{ m s}^{-1}$  for the radial velocity.

For the SCL, the radial velocity data from the three radars were divided into three subsets with dense, medium, and coarse observational distributions. The percentages of the data coverage for the coarse, medium, and high densities are 10%, 30%, and 60%, respectively (see S-Pol radar data in Fig. 5 as an example).

### c. Numerical experiments

In this study, all the experiments used the WRF Model V4.0, with triply nested domains (Fig. 1b) and two-way interactions. The horizontal grid spacings for domains 1–3 are 27, 9, and 3 km, respectively. There are 51 vertical levels, and the model top is at 50 hPa. A 62-member ensemble was initialized by two sets of 31-member global ensembles sourced from the NCEP Global Ensemble Forecast System (GEFS) data at 1200 UTC and 1800 UTC 5 June, respectively. After all the ensemble members had spun up to 2100 UTC 6 June, radar assimilation was conducted for 6 h with a 12-min analysis cycle for the innermost domain (at a 3-km grid spacing). Owing to two-way interactions, domain 3 data overwrote those in the same region in domains 1 and 2. For each experiment, after a 6-h analysis cycle, a 6-h deterministic forecast was conducted using the analysis ensemble mean at 0300 UTC 7 June, with the boundary conditions taken from the NCEP GEFS. The physical parameterization schemes used in WRF forecasts include the Goddard Cumulus Ensemble (GCE) model micro-physics scheme (Tao et al. 1989), the Yonsei University (YSU) planetary boundary layer scheme (Hong et al. 2006),

the RRTM for GCMs (RRTMG) radiation scheme (Iacono et al. 2008) for both longwave and shortwave radiations, the Unified Noah land surface model (Chen and Dudhia 2001), and the Kain–Fritsch cumulus parameterization (Kain 2004), which were applied to domains 1 and 2 only. Notably, the 12-min ensemble forecasts during the analysis cycles and the 6-h deterministic forecasts used the same model configuration and domains.

Two experiments were conducted to assimilate the radial velocity and reflectivity of the radar. Radar reflectivity is assimilated via convective-scale localization in both experiments. This is because, for convective-scale precipitation systems, the characteristics of the hydrometer variables are presented as small-scale features. Thus, the standard convective-scale localization used for the assimilation of reflectivity reflects the scale of the hydrometeors for convection. However, for the radial velocity, one experiment uses convective-scale localization (RDA), whereas the other uses multiscale localizations (i.e., the SCL method; MRDA). The radial velocity is a combination of the convective-scale wind perturbations to the background synoptic flow, and thus, multiscale localizations will be needed. The impact of multiscale corrections on heavy rainfall forecasts can be evaluated by comparing the analysis and forecasts between RDA and MRDA.

In each numerical experiment, the convective-scale localization applied to the RDA experiment is 12 km horizontally and 4 km vertically, following a standard setup (Tsai et al. 2014; Wu et al. 2020). For MRDA, the SCL method is applied to multiscale corrections for which the large-to-small horizontal localization scales in three iterations are 500, 150, and 12 km, respectively, and only three components of winds and geopotential height are updated. To update other prognostic variables, such as moisture and hydrometeors, a convective-scale localization (i.e., 12 km) was used. The choice of the updated variables was optimized based on previous studies (Lin et al. 2022; Chung et al. 2013). The uncertainties of wind and geopotential are related to the variations in the large-scale weather system, whereas the hydrometers are related to the thermodynamic process of convection. Notably, the temperature field was not updated since assimilating the radial velocity or reflectivity does not provide clear temperature corrections through the cross-variable error correlation. Nevertheless, the temperature variable was adjusted during the forecast because of the corrections to other variables.

Data from “quantitative precipitation estimation and segregation using multiple sensors (QPESUMS; Chang et al. 2021)” provided by Taiwan’s CWA are used for analysis and forecast verification. QPESUMS offers calibrated, gridded observations ( $0.125^\circ \times 0.125^\circ$  resolution), including radar reflectivity and rainfall accumulation.

## 4. Results

### a. Convection and rainfall forecasts initialized at 0300 UTC 7 June

We first assess the forecast benefit of applying multiscale corrections to radar radial velocity assimilation by comparing the forecast differences between RDA and MRDA. Figure 6

shows the forecasted composite reflectivity from MRDA (top) and RDA (bottom). Compared with RDA, MRDA produces stronger reflectivity during the first 3-h forecast from 0300 to 0600 UTC 7 June. In particular, more convective cells actively develop over the western coast in MRDA, although these cells might not exactly resemble the location and intensity of those in the observations (Fig. 3). The MRDA 1-h reflectivity forecast reveals more intense line convection off the northwestern coast, with more organized low-level convergence over the frontal region (indicated by the blue box area in Fig. 6a vs Fig. 6d). Furthermore, compared with the RDA wind field, the MRDA forecast produces a stronger westerly wind component over the ocean near the northwestern ( $24.7^\circ$ – $25.2^\circ\text{N}$ ) and southwestern ( $\sim 23^\circ$ – $23.5^\circ\text{N}$ ) coasts of Taiwan (Fig. 6a vs Fig. 6d) and a stronger southerly component along the coast of central Taiwan (Fig. 6b vs Fig. 6e, near  $24^\circ\text{N}$ ,  $120.5^\circ\text{E}$ ). The convection initiated at the coast of central Taiwan rapidly intensified, moved northward, and merged with the bent-line convection along the northwestern coast (Fig. 6c), which was originally nearly linear off the northwestern coast only 3 h before.

Compared with an experiment initialized with FNL data (i.e., without the assimilation of radar data; figure not shown), radar assimilation with short localization (i.e., RDA) successfully improves very short-term (6-h) rainfall prediction (Fig. 7). The use of the SCL method in MRDA further improves the accumulated rainfall. MRDA produces more rainfall than does RDA during the first 3-h forecast, such as the heavy rainfall in northern and central Taiwan, which better agrees with the observations (Fig. 7a vs Fig. 7b vs Fig. 7c). The heavy rainfall in MRDA is located closer to the coast, as observed. Furthermore, the 3–6-h MRDA forecast also better captures the northeast–southwest elongated rainband in northern Taiwan and the rainfall north of  $23.5^\circ\text{N}$  near the eastern coast (Fig. 7d vs Fig. 7e vs Fig. 7f). The forecast results suggest that the SCL method provides essential multiscale corrections for analysis (i.e., initial conditions), which leads to rapid coastal convective development and extends the benefit of radar data assimilation to later forecast hours. MRDA has objectively better rainfall forecast skills than RDA, which is described in detail in section 6.

Next, we discuss how initial conditions (i.e., analysis at 0300 UTC 7 June) contribute to forecast differences between RDA and MRDA and the mechanisms that lead to the heavy rainfall event.

### b. Analysis and mechanisms

As shown in Figs. 8d and 8h, reflectivity analyses from MRDA and RDA are similar because of the assimilation of radar reflectivity in both experiments, but their low-level kinematic fields are notably different, as shown in the low-level streamline and convergence fields (Figs. 8a–c vs Figs. 8e–g), which leads to different convection development between the two experiments after free forecasting.

#### 1) KINEMATICS

Two major kinematic features that contribute to the heavy rainfall in Taiwan are of great interest. The first feature is the

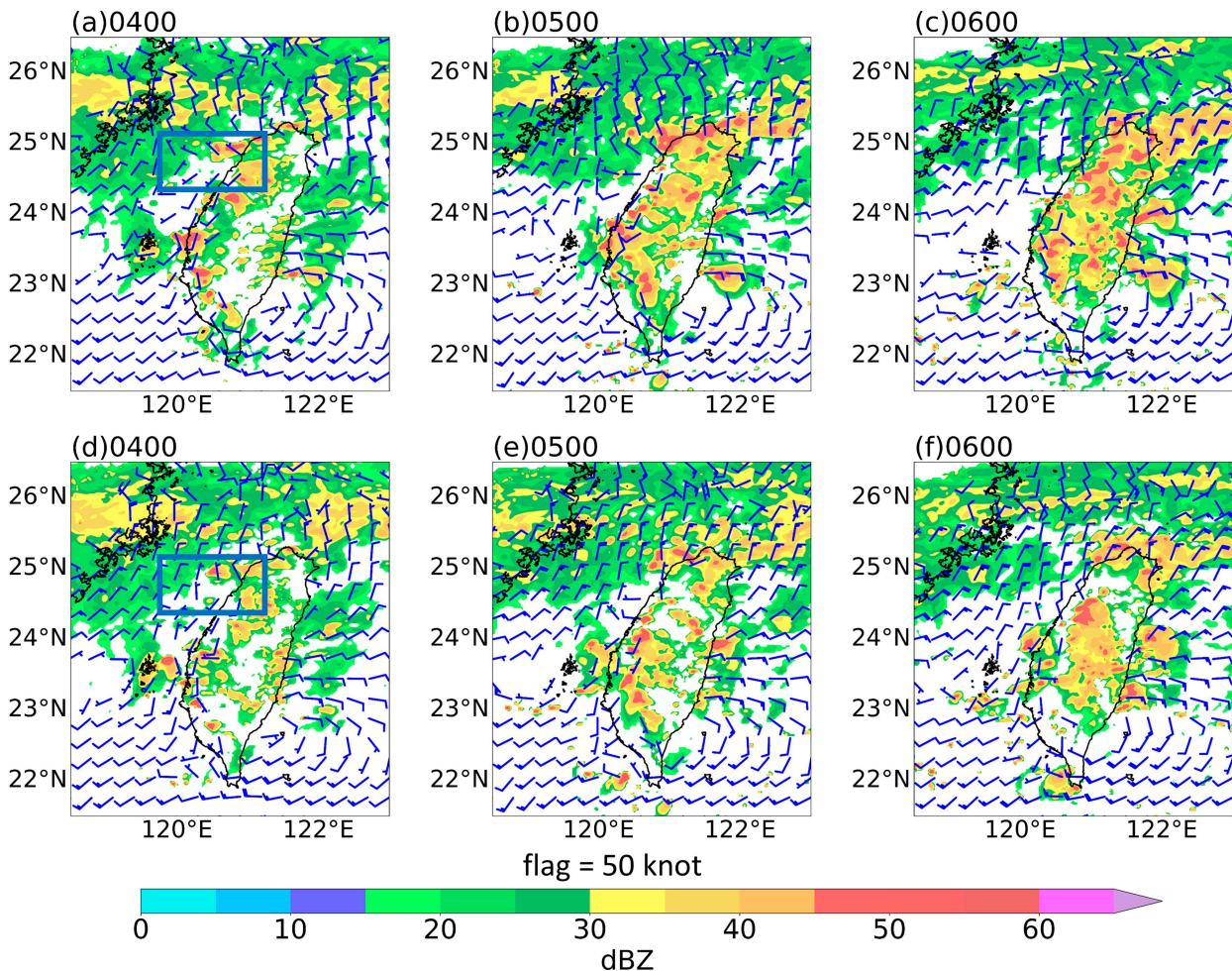


FIG. 6. Column maximum reflectivity and 975-hPa wind forecasts for (top) MRDA and (bottom) RDA from 0400 to 0600 UTC 7 Jun 2022. The column maximum reflectivity is the composite of each column's maximum reflectivity. The blue boxes indicate the frontal convergence zone near the surface.

existence of a low-level mesoscale vortex off the coast of western Taiwan. The mesoscale vortex plays a critical role in the convergence zone offshore of southwestern Taiwan (near 23.5°N in Fig. 8c), and the convergence is stronger in MRDA than in RDA analysis. Both MRDA and RDA analyses produce the mesoscale vortex, which is very shallow (below 925 hPa). However, the characteristics of their represented vortices are quite different. The mesoscale vortex in RDA is narrower and more elongated and is oriented in the northeast-southwest direction. On the other hand, MRDA has a broader, more intense, east-west-oriented vortex with a clear westerly wind component from Penghu Island to the southwestern coast of Taiwan (see Fig. 1a for the location of Penghu Island). Moreover, the vortex center in the MRDA analysis is located offshore of central Taiwan (approximately 24.25°N), whereas it is located further north (approximately 24.6°N) in RDA. The differences in the orientation, location, and shape of the vortex lead to different convergence features and moisture transport toward the coast of western Taiwan and the development of convective cells (Fig. 6).

The second feature is the convergence zone located off the coast of northwestern Taiwan. The convergence zone is related to the southward moving front and is decisive in the development of the line convective system there (Fig. 6). Compared with RDA, this convergence zone is better organized in the MRDA analysis, extending from the surface to 850 hPa.

As we will further demonstrate, we argue that the corrections for the shallow mesoscale vortex west of central Taiwan and the convergence over the frontal zone outside northwest Taiwan are critical features in the analysis that lead to the rapid development of intense coastal rainfall and are established more clearly with the multiscale corrections in MRDA.

#### (i) Mesovortex offshore of central Taiwan

The existence and characteristics of the low-level mesoscale vortex (mesovortex) in the initial conditions of MRDA play a key role in the heavy coastal rainfall event. Compared with RDA, the modification of the vortex in the MRDA analysis started at the first analysis time (2100 UTC 6 June), as shown in the wind increments (Fig. 9a vs Fig. 9d). Given the same

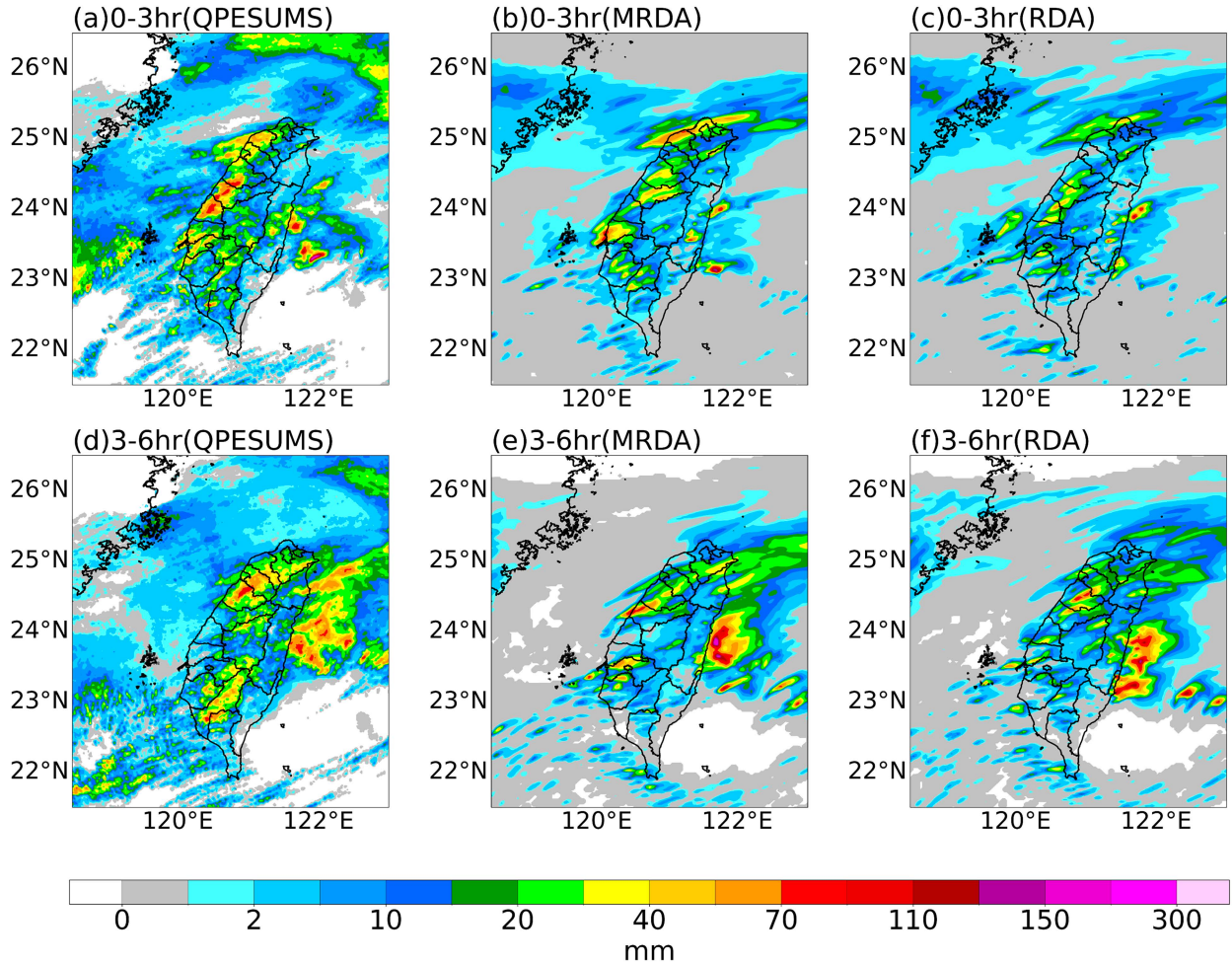


FIG. 7. Three-hourly accumulated rainfall from (top) 0300 to 0600 UTC and (bottom) 0600 to 0900 UTC 7 Jun from (a),(d) QPESUMS and model forecasts from (b),(e) MRDA and (c),(f) RDA initialized by the ensemble analysis mean at 0300 UTC 7 Jun.

background ensemble at this time, the SCL method provides broader-scale westerly corrections offshore of southwestern Taiwan and southerly corrections off the coast of central Taiwan (Fig. 9a). As a result, these wind corrections extend the mesovortex circulation eastward, reshaping it into broader circulation at low levels. After 48 min (four analysis cycles), the MRDA analysis at 2148 UTC provides northerly wind corrections in the radar data void region northwest of Penghu Island (Fig. 9b); this helps relocate the mesovortex center northeastward and closer to the coast (Fig. 9c). With the commonly adopted scanning strategy, radar radial wind observations ( $V_{rs}$ ) are very limited at low levels because of the elevation angle. However, the low-level wind correction over the data void region north of Penghu can be derived via the background error correlation between the model  $V_r$  and winds in this region with the use of a long localization in MRDA, which increases the convergence along the western coast up to  $24^\circ\text{N}$  due to westerly wind corrections. In contrast, RDA can provide corrections only at and near regions with radar data and produces no corrections in the data void

region (Figs. 9d,e), which cannot help relocating the shallow mesoscale vortex northeastward (Fig. 9f). Even though there are data away from the radar site, the data are from a higher altitude due to the elevation angle, and no correction can be derived to help relocate the shallow mesovortex northeastward at 2148 UTC in RDA (Fig. 9f).

Unfortunately, not many observations are available to directly evaluate the existence and characteristics of the shallow mesovortex. The only independently available observations for vortex verification include the surface station data at Penghu and the radiosonde sounding at Magon on Penghu Island, which is located at the south-southwest edge of the vortex. Compared with the sounding data at 0000 UTC 7 June, the wind direction in the MRDA analysis revealed westerly flow below 500 m, which agrees better with the observations (Fig. 10). The surface station also experienced a nearly westerly wind at this time. On the other hand, the wind direction in the RDA analysis over this region is more southwesterly. The comparison results provide some confidence in the location, shape, and orientation of the mesovortex in the MRDA

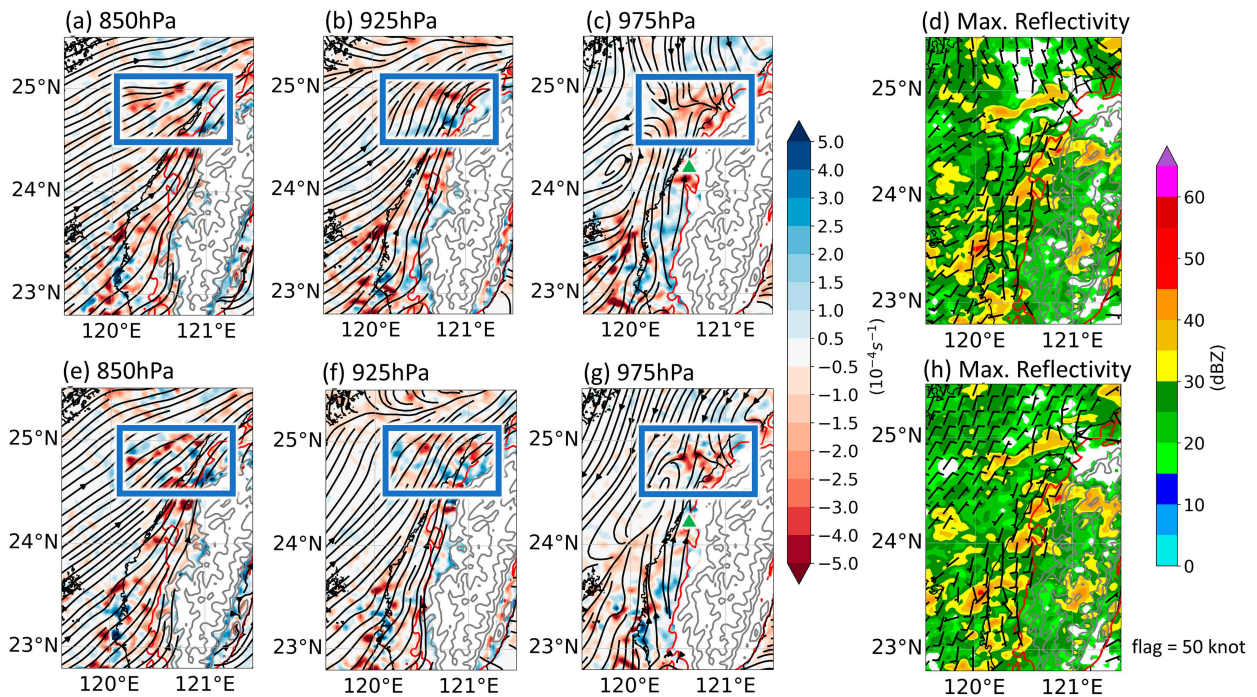


FIG. 8. Streamlines and convergence (shading;  $10^{-5} \text{ s}^{-1}$ ) at (a) 850, (b) 925, and (c) 975 hPa and (d) maximum reflectivity and 975-hPa wind bars from MRDA analysis at 0300 UTC 7 Jun. (e)–(h) As in (a)–(d), but for the RDA analysis. The green triangles in (c) and (g) indicate the location of the Dadu Terrace. The blue boxes indicate the location of the frontal zone.

analysis. Nevertheless, without any direct measurements of the mesoscale vortex itself, we can only argue for the role of the vortex in this heavy rainfall event based on the comparison of reflectivity and rainfall characteristics between the observations and model predictions. The discussion below provides one example.

As shown in Fig. 8c, the localized convergence near the Dadu Terrace (the green triangle) is stronger in the MRDA analysis. Southwest of the Dadu Terrace, the wind flow off the coast is dominated by the mesoscale vortex, which provides a stronger near-surface westerly wind component (Fig. 8d), creating convergence at the coast due to the surface friction difference between land and ocean. In combination with the southerly flow along the coast of western central Taiwan, convergence is enhanced ( $\sim 120^\circ\text{E}$ ). This results in more intense convection echoed by the forecasted reflectivity (Figs. 6a–c) and more rainfall (Fig. 7b) along the coast of central Taiwan. Therefore, the intensity and location modifications of the mesoscale vortex by the SCL method are the key features leading to better convection forecasts in the coastal region of central Taiwan.

Notably, the mesovortex moved inland 2 h after the forecast (figure not shown) and became difficult to identify. In addition, owing to the limited near-surface observations from radars, the characteristics of the mesoscale vortex may possess some uncertainty in terms of size, location, and time; therefore, the location and intensity of heavy rainfall forecasts may still have some degree of error compared with the observations.

#### (ii) Frontal convergence zone offshore of northwestern Taiwan

Compared with RDA, MRDA establishes a stronger frontal convergence zone in northwestern Taiwan, which extends further west at 0300 UTC 7 June (Fig. 8). The volume-averaged convergence around the frontal region (boxes in Fig. 8) from the surface to 850 hPa is about  $-4.2 \times 10^{-5} \text{ s}^{-1}$  for RDA and  $-6.0 \times 10^{-5} \text{ s}^{-1}$  for MRDA. When the front moved southward and approached Taiwan, the assimilation of Vr at 0248 UTC 7 June with the SCL method generated northerly wind corrections behind the frontal rainband offshore of northwestern Taiwan ( $\sim 25^\circ\text{N}$  in Fig. 11a). Although RDA also reveals some northerly corrections, they are rather limited near the S-Pol radar (Fig. 11b). Moreover, to the north of the northerly wind increment area, MRDA exhibits westerly wind corrections (i.e.,  $25^\circ\text{N}$ ), which changes the northeasterly flow (background) to nearly northerly (analysis) north of the front. These westerly corrections result from assimilating the Vr of the WuFen radar (Fig. 1a) with the SCL method and cannot be derived in the RDA analysis, which reveals northeasterly flow north of the front. At the same time, the MRDA analysis also reveals a broader, more east–west-oriented mesoscale vortex to the south of the front, contributing to the easterly flow in this region. Combining the easterly flow south of the front and the stronger northerly wind component north of the front, the convergence zone in MRDA is stronger, more concentrated, and extends further west offshore, enhancing the temperature gradient at the frontal zone (comparing the box area in Fig. 11c with Fig. 11d). This maintains stronger and more concentrated line

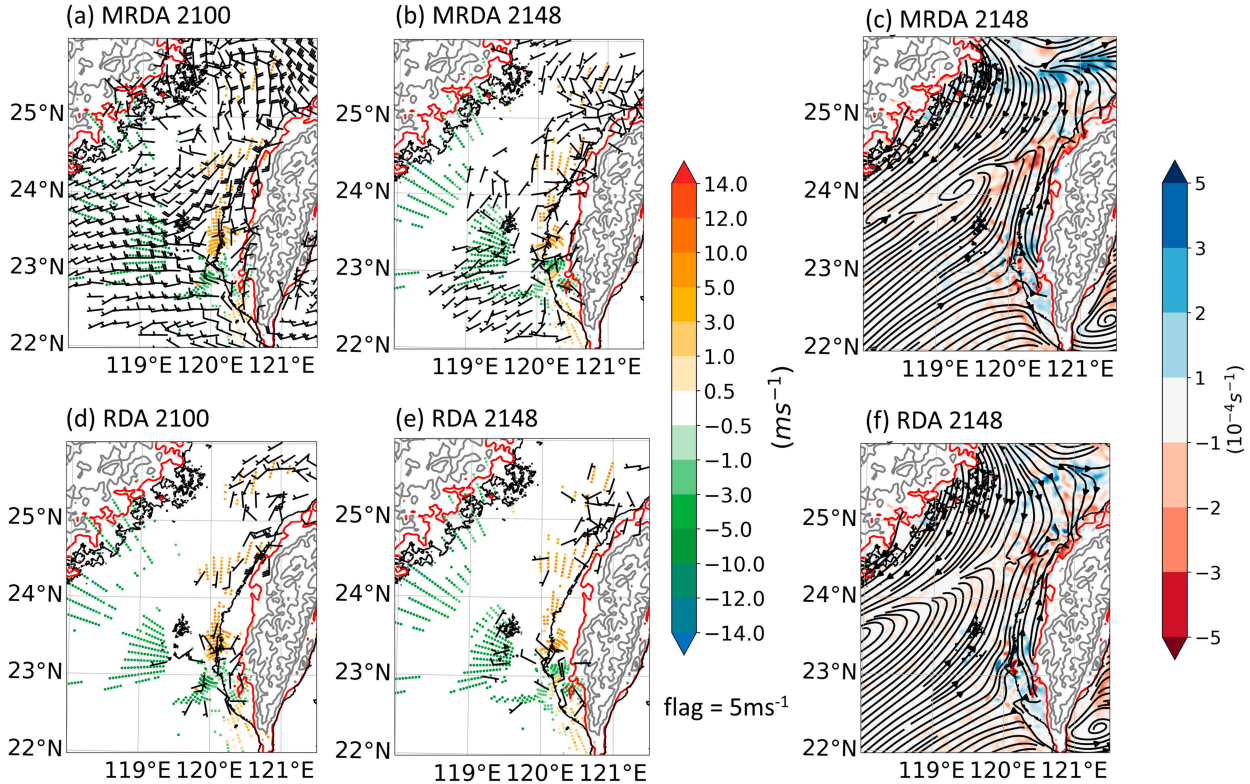


FIG. 9. Wind increments of MRDA at 975 hPa at (a) 2100 and (b) 2148 UTC 6 Jun. The color shading denotes the superrobed  $V_r$  of RCCG. (d), (e) As in (a) and (b), but for RDA. Streamline and convergence (shading) of the (c) MRDA and (f) RDA analyses at 975 hPa at 2148 UTC 6 Jun.

convection along the front, which better supports coastal convection later in the forecast.

## 2) MOISTURE FLUX AND CONVECTIVE INSTABILITY

While kinematic fields may influence these convective systems, thermodynamically influential fields, including the moisture flux, also play an essential role in this heavy rainfall event. Although the moisture variable in both MRDA and RDA is updated with convective-scale localization, the

differences in the wind corrections in MRDA and RDA greatly affect the moisture transport over the western coast of Taiwan, and their differences accumulate during data assimilation cycling. With the enhancement of the westerly component north of Penghu Island within the planetary boundary layer (PBL) and the relocation and reshaping of the mesoscale vortex offshore of central Taiwan at 2148 UTC 6 June, the low-level moisture transport into western Taiwan in the MRDA analysis is clearly augmented. With the accumulated impact, the MRDA analysis at 0300 UTC 7 June reveals a larger area for high moisture fluxes from offshore southwestern Taiwan to the coast of central Taiwan (Fig. 12a vs Fig. 12b) and thus has a larger area of high equivalent potential temperature ( $>350$  K) near the surface (Fig. 12c vs Fig. 12d).

The change in the low-level equivalent potential temperature can modify the convective instability (i.e., the vertical gradient of the equivalent potential temperature) and thus convection development. Figure 13 shows the Hovmöller diagram of the low-level convective instability, represented by the equivalent potential temperature difference between 850 and 975 hPa, along  $24.36^\circ\text{N}$  from both forecasts. Compared with RDA, MRDA produces greater convective instability offshore in the initial conditions (figure not shown); the convective instability is transported into the coastal region once the forecast starts and lasts until 0600 UTC. As discussed earlier, the stronger low-level westerly wind component west of

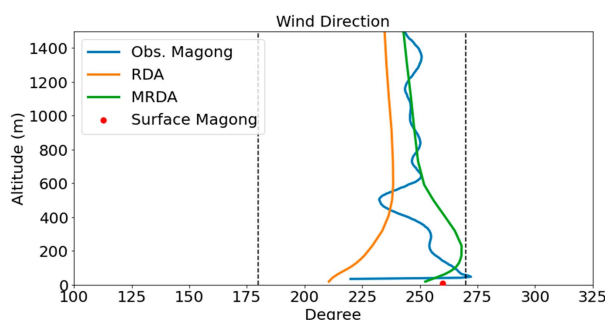


FIG. 10. Vertical profile of the wind direction from the radiosonde at Magong (blue line), RDA (orange line), and MRDA (green line) at 0000 UTC 7 Jun 2022. The dots are the wind direction observations from the surface station at Magong in Penghu.

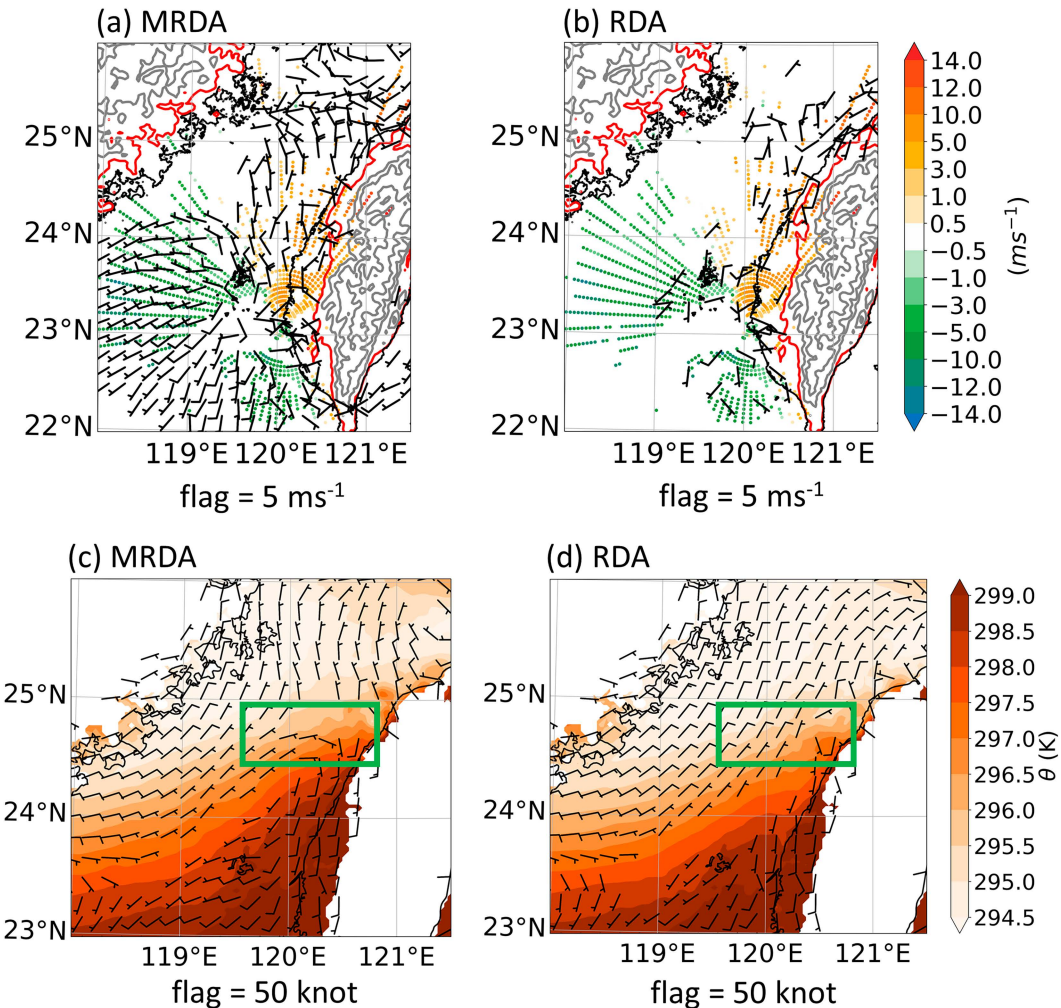


FIG. 11. The wind increments of (a) MRDA and (b) RDA at 975 hPa at 0248 UTC 7 Jun. The color shading denotes the superrobbed  $V_r$  of S-Pol. Wind barbs and potential temperatures (shading; K) of (c) MRDA and (d) RDA at 1000 hPa at 0300 UTC 7 Jun. The green boxes indicate the convergence zone near the front.

central Taiwan and stronger southerly wind at the western coast in MRDA induce stronger convergence along the western coast. The convergence encourages upward motion with high moisture flux and convective instability from the southwest into the coastal area, which can support the development of rapid convection, leading to heavy rainfall along the western coast.

The differences in precipitation and convection between RDA and MRDA over the western coast are attributed to changes in both the wind (e.g., convergence) and moisture fields, resulting in notable differences in the moisture flux and convective instability. We hypothesize that the role of the low-level flow change, which is caused mainly by the meso-scale vortex, dominates the moisture change in heavy rainfall production over the western coast. To untangle the moisture impact from wind, we conduct a new experiment (called RDA\_ModQv), which replaces RDA's moisture field with MRDA's moisture field in the upstream region of the third

(southwest) quadrant of domain 3, with central Taiwan as the origin. In other words, we provide abundant moisture while the weak convergence at the coast remains the same as that in RDA. The results show that RDA\_ModQv produces rainfall more similar to that of RDA (Fig. 14a vs Fig. 7c), as the moisture is transported toward the northeast, instead of more eastward, which is required for intensifying convection and heavy rainfall over the western coast. Compared with RDA, RDA\_ModQv can slightly improve rainfall prediction for longer forecast hours (Fig. 14b vs Fig. 7f). This finding supports our hypothesis that the dynamic field in MRDA plays a dominant role in heavy rainfall over western Taiwan.

## 5. Sensitivity experiments

Under the WLRAS-SCL framework, two sets of sensitivity tests are conducted to further examine the impact of data

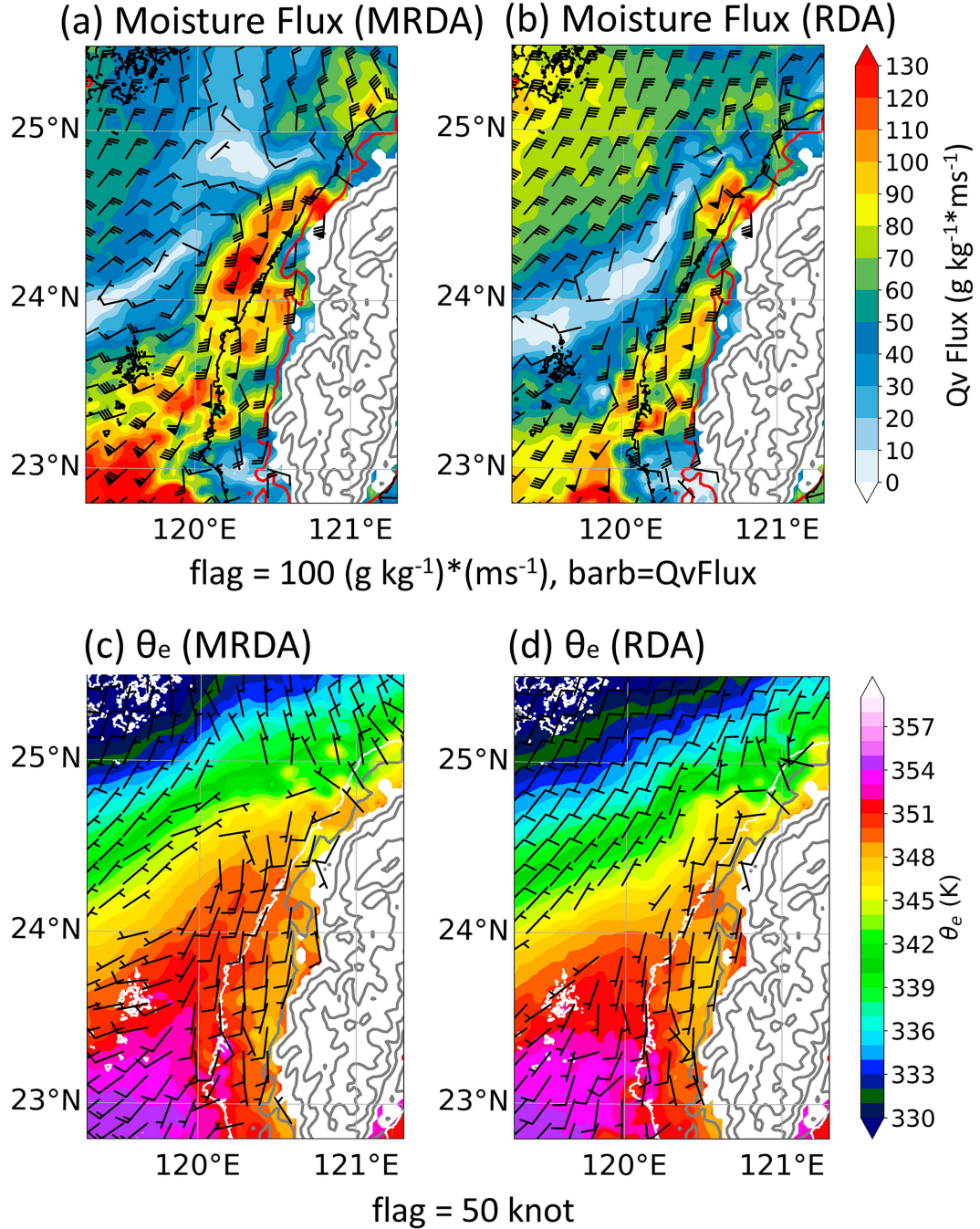


FIG. 12. (a) MRDA and (b) RDA moisture fluxes at 975 hPa at 0300 UTC 7 Jun. The wind barbs and equivalent potential temperature ( $\theta_e$ ) of (c) MRDA and (d) RDA analyses at the same time.

from different radars and the use of multiscale localization in water vapor corrections on heavy rainfall forecasts.

#### a. Radar data

In the previous section, we identified several important features in the MRDA analysis and forecast compared with the RDA analysis and forecast. In this subsection, we conduct

two sensitivity experiments to investigate how these features are attributed to data assimilation from two radars by removing either Chigu (named MRDA\_nCG) or S-Pol (named MRDA\_nSP) data. Other than that, the remaining experimental design is identical to that of MRDA.

Compared with the relocated and reshaped mesoscale vortex in the MRDA analysis at 2148 UTC 6 June, MRDA\_nCG does not exhibit such a feature in its analysis. Without the

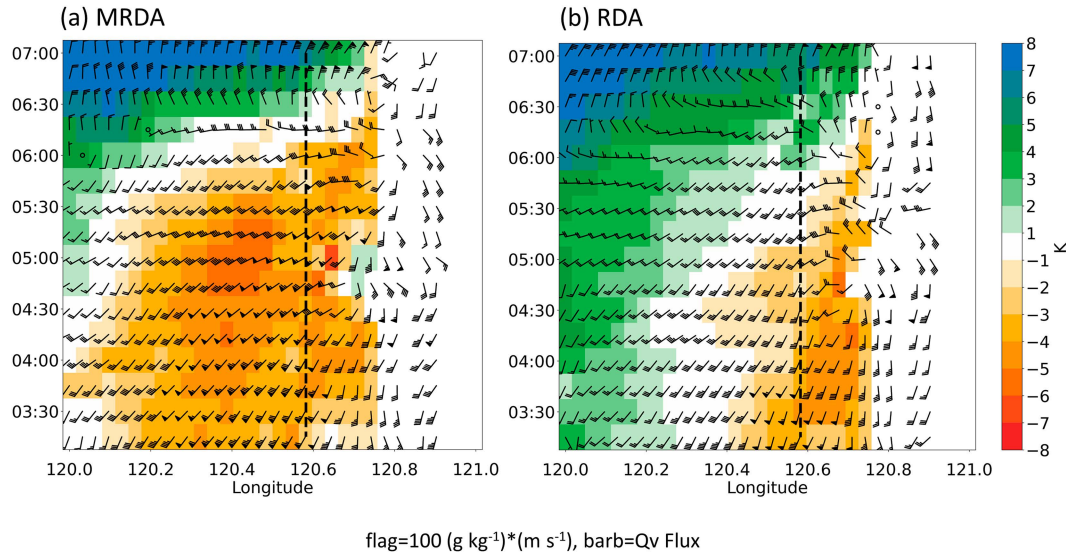


FIG. 13. Hovmoller diagram of the equivalent potential temperature difference (shading; K) between 850 and 975 hPa and the moisture flux (wind barbs) at 950 hPa along 24.36°N from 0300 to 0700 UTC 7 Jun for (a) MRDA and (b) RDA. The dashed line indicates the location of the coast.

westerly wind corrections resulting from the assimilation of Chigu's radial velocity, the wind remains from a southerly direction southwest of Taiwan, and convergence off the coast is reduced (Fig. 15a vs Fig. 8c). This confirms that the westerly wind corrections in a broader area near Penghu via the assimilation of wind from the Chigu radar help relocate and reshape the offshore mesovortex, which can further help establish more convergence at the coast. Consequently, moisture transport is suppressed in MRDA\_nCG, as indicated by the clearly reduced moisture flux southwest of Taiwan (Fig. 15b vs Fig. 12a). Without higher moisture transport to enhance convective instability, convection over southwestern Taiwan is much weaker and

propagates into central Taiwan (figure not shown). As a result, the forecast ability of MRDA\_nCG is notably poorer than that of MRDA. Although the front-associated rainband remains over northern Taiwan from 0300 to 0600 UTC, MRDA\_nCG's forecast loses most of the heavy rainfall over the western coast (Figs. 16a,d vs Figs. 7b,e).

Without assimilating the S-Pol radar data, the MRDA\_nSP analysis at 975 hPa reveals northeasterly winds behind (i.e., north of) the frontal zone at 0300 7 June compared with the northerly winds in MRDA (Fig. 15f vs Fig. 8d). Consequently, the frontal convergence zone offshore of northwestern Taiwan is weaker in MRDA\_nSP (Fig. 15d vs Fig. 8c). In addition,

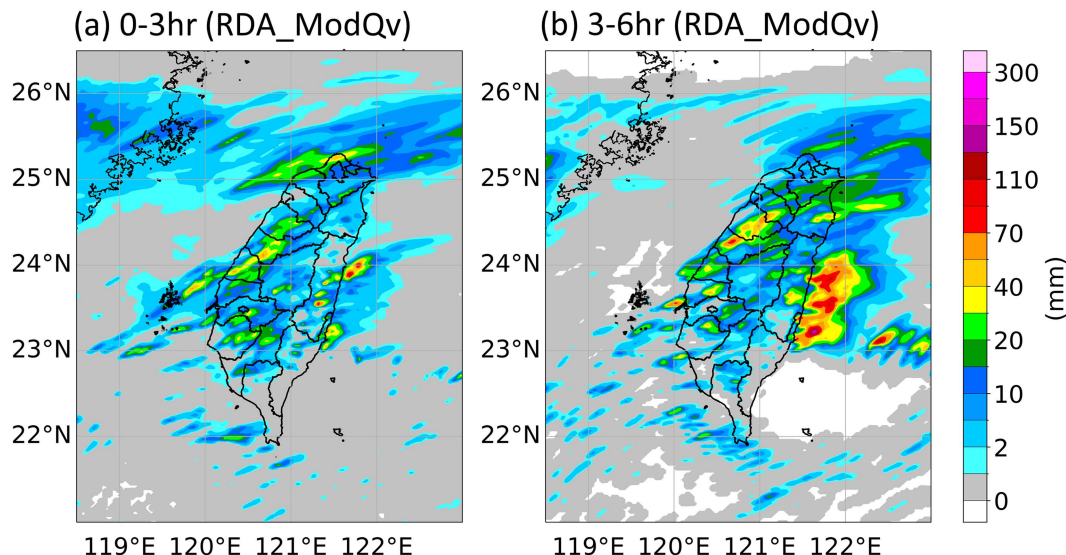


FIG. 14. As in Fig. 7, but for (a),(b) RDA\_ModQv.

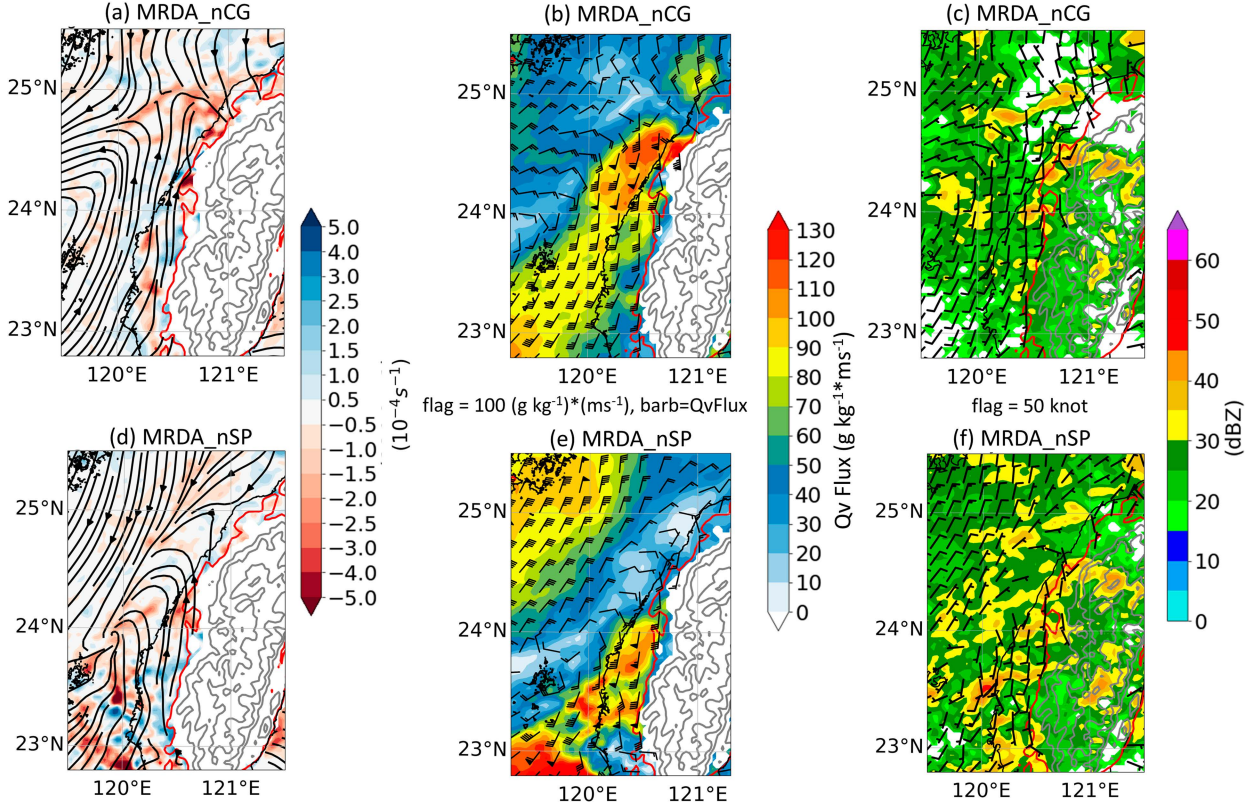


FIG. 15. The 975-hPa streamlines and convergence (shading;  $10^{-4} \text{ s}^{-1}$ ) for (a) MRDA\_nCG and (d) MRDA\_nSP at 0300 UTC 7 Jun. Moisture flux (shading;  $\text{g kg}^{-1} \text{ m s}^{-1}$ ) analysis at 975 hPa at the same time for (b) MRDA\_nCG and (e) MRDA\_nSP, respectively. (c),(f) As in (b) and (e), but for the 975-hPa wind barbs and column maximum reflectivity.

while the mesoscale vortex center in the MRDA\_nSP analysis can shift toward the western coast at this time, its shape and location (further south) are clearly different from those in MRDA. The in-concert effect of the frontal zone and mesoscale vortex in MRDA cannot be produced in MRDA\_nSP; thus, the moisture flux becomes much weaker (Fig. 15e). As a result, the line convection over the frontal region cannot be well established (Fig. 15f). As mentioned earlier, without line convection moving inland and its tail appressing the coast (Fig. 3), cell merging and rapid intensification cannot be reproduced. The convection along the coast of northwestern Taiwan decays quickly within the next hour (figure not shown).

Without convergence and line convection off northwestern Taiwan in MRDA\_nSP, the rainfall over northwestern Taiwan is greatly reduced during the first 3-h forecast from 0300 to 0600 UTC (Fig. 7b vs Fig. 16b). Despite coastal rainfall, the elongated southwest–northeast rainband during the second 3-h forecast is weaker (Fig. 7e vs Fig. 16e). The differences between MRDA and MRDA\_nSP imply how important the S-Pol radar data, the additional radar from the TAHOPE/PRECIP field campaign, are in recovering the frontal convergence offshore of northwestern Taiwan and the sustained presence of western coastal convection and rainfall.

#### b. Impact of large-scale moisture update

As MRDA results in greater moisture transport onto the western coast of Taiwan, this feature is attributed to the wind field modified by the SCL method since only convective-scale localization is used in the moisture corrections in MRDA. The choice of localization for the moisture update is due to the moisture not being directly observed in the assimilated data, relying instead on the error correlation with the modeled radial wind. However, moisture updates in ensemble data assimilation are complicated by the fact that the background error correlation between moisture and the radial wind can be opposite to that between moisture and reflectivity (Yang et al. 2020). In addition, without a direct relationship, the error correlation between moisture and radial velocity or reflectivity is more easily contaminated by sampling error; thus, the use of convective-scale localization is often recommended (Wu et al. 2020).

Nevertheless, it is of great interest to use the SCL method in the moisture field and evaluate its benefit in heavy rainfall forecasting, given the abundant moisture transport in this case. Thus, we conducted another sensitivity test, named MRDA\_Qv, whose experimental setting is the same as that of MRDA, except that the SCL method is used to derive the moisture correction when the radial wind is assimilated. We note that the moisture is also updated by the assimilation of

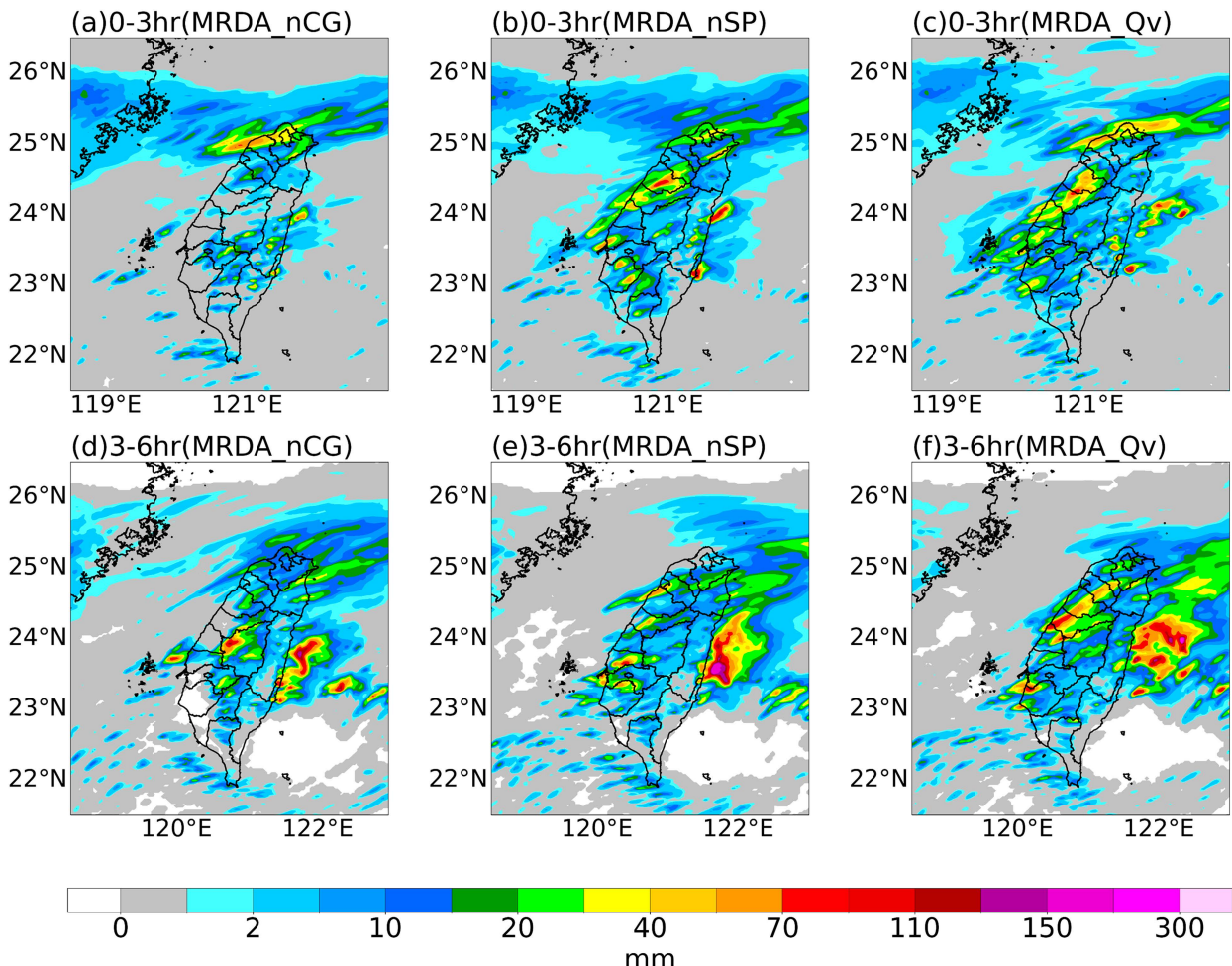


FIG. 16. As in Fig. 7, but for (a),(d) MRDA\_nGG, (b),(e) MRDA\_nSP, and (c),(f) MRDA\_Qv forecasts.

reflectivity with convective-scale localization, which is the same as that in MRDA and RDA.

Compared with MRDA, MRDA\_Qv has higher moisture increments that extend to a broader area offshore of the western coast at the first analysis time (Fig. 17b vs Fig. 17a at 2100 UTC 6 June), and this moist increment is even more apparent at 850 hPa (Fig. 17f), where the moisture flux is at its maximum. This leads to a greater enhancement of moisture transport into the coastal area. Combined with the effect of wind, the moisture transport from MRDA\_Qv is consistently greater than that from MRDA off the western coast during the analysis period. Before the forecast initialization at 0300 UTC 7 June, the moisture increment was also more evident within the boundary layer south of the Penghu area in the upstream region of southwestern Taiwan (Fig. 17h vs Fig. 17g) and thus had a large impact on rainfall prediction.

Compared with MRDA (Figs. 7b,e), the rainfall forecast is improved in MRDA\_Qv (Figs. 16c,f). During the first 3-h forecast, the intensity of the coastal rainfall increases in MRDA\_Qv, with an amplitude closer to what was observed.

The benefit of using SCL in the moisture update in MARDA\_Qv is more evident for the last 3-h forecast from 0600 to 0900 UTC 7 June. Specifically, the heavy rainfall magnitude and coverage in the southwest-northeast-oriented rainband in northern Taiwan and the heavy rainfall east of central Taiwan in MRDA\_Qv better resemble the observations because of the use of large-scale localization in moisture corrections.

The benefit of multiscale moisture update is further justified by comparing the total precipitable water (TPW) analyses between MRDA and MRDA\_Qv with observations. Notably, the wind analyses between these two experiments are generally comparable (figure not shown). Although the satellite-based TPW is lower off the western coast, the zenith tropospheric delay (ZTD)-based TPW (Yeh et al. 2016) clearly exhibits local high TPW values over the western coast near 23.5° and 24°N, and TPWs from both MRDA and MRDA\_Qv correspond well with these observed maxima. Compared with the satellite-derived TPW (Fig. 18a), the MRDA TPW pattern near Taiwan shows good agreement overall but substantially underestimates the values west of

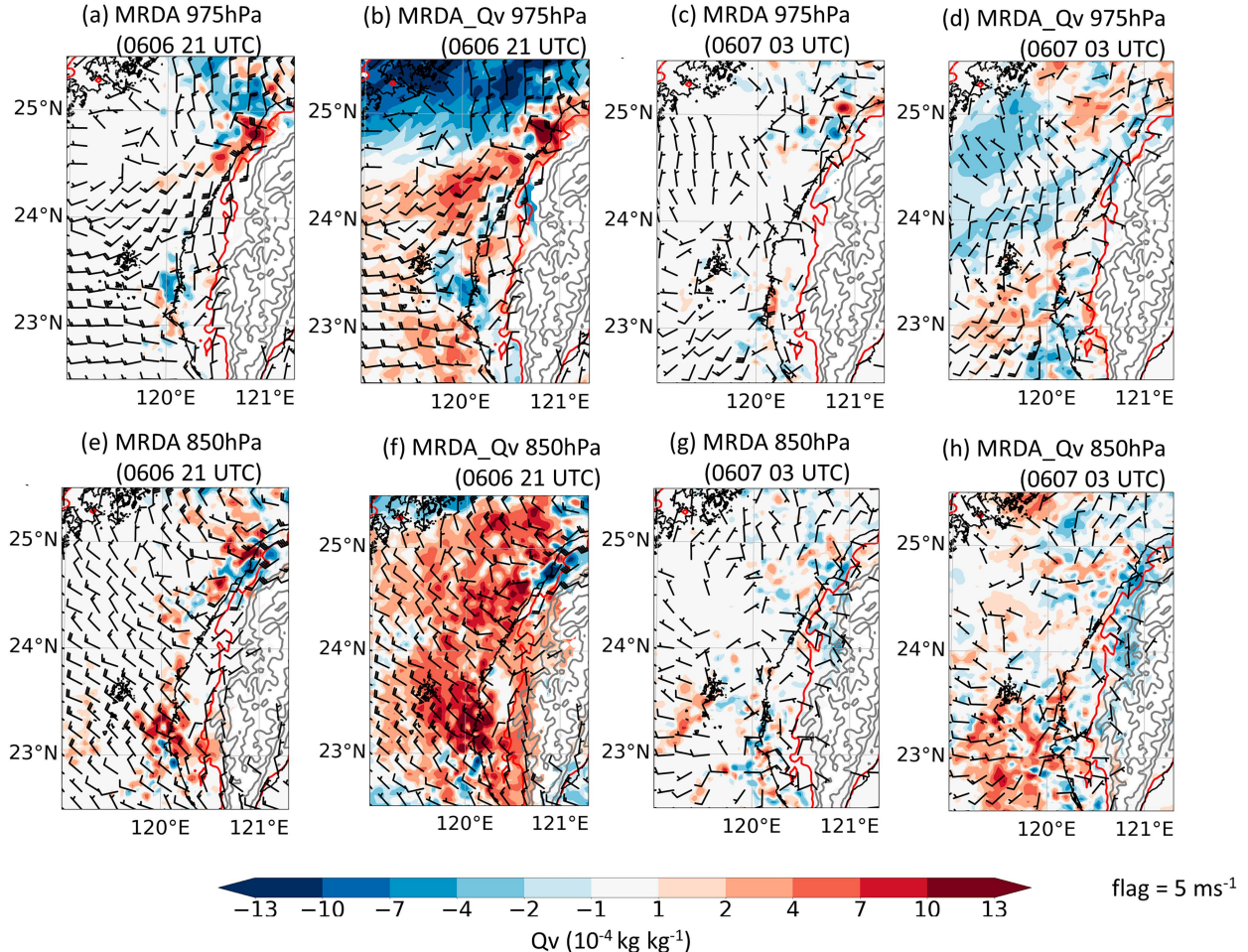


FIG. 17. (a) MRDA and (b) MRDA\_Qv wind barbs and moisture increment (shading;  $10^{-4} \text{ kg kg}^{-1}$ ) at 975 hPa at 2100 UTC 6 Jun. (c), (d) As in (a) and (b), but at 0300 UTC 7 Jun. (e)–(h) As in (a)–(d), respectively, but at 850 hPa.

the Penghu area. MRDA\_Qv further enhances the TPW analysis offshore of southwestern Taiwan and north of the front at 0300 UTC 7 June (Fig. 18c). The moisture enhancement explains the better rainfall forecast of MRDA\_Qv (Figs. 16c,f).

Despite the improved rainfall forecast in Taiwan, the moisture analysis in MRDA\_Qv revealed a slight reduction off the coast of eastern China and a clear increase north of the front compared with MRDA. These adjustments, which are far from the radar observations, actually degrade the accuracy of the MRDA\_Qv TPW compared with satellite-derived estimates. This finding echoes the earlier discussion that the ensemble-based background error correlation between moisture and radial wind is less robust and can be contaminated by sampling errors, particularly at farther distances. Although adjustments at farther distances do not affect the rainfall forecast in Taiwan because of the wind direction, the comparison suggests that short localization for moisture update is a safer strategy. Ultimately, a better solution is to measure moisture directly to provide reliable moisture correction.

## 6. Forecast skills

### a. Forecast initialized at 0300 UTC 7 June

To quantitatively evaluate rainfall prediction, the fractions skill score (FSS; Roberts and Lean 2008), a spatial verification technique, is first used to compare the precipitation characteristics between forecasts and observations. Given a threshold (e.g., accumulated rainfall greater than 10 mm), FSS measures the squared difference in the exceedance grid number between forecasts and observations above the threshold over a neighborhood region. The calculation is performed separately at each grid point and then averaged over the targeted area. The size of the neighborhood varies gradually from small to large to address the question of at which scale the observed feature will be visible in the forecast and how skillful the forecast is at that scale. The FSS value ranges from 0 to 1, and the higher the value is, the better the forecast skill is. In this study, the evaluation focuses on a limited area covering Taiwan ( $22^{\circ}$ – $25.5^{\circ}$ N and  $119.5^{\circ}$ – $122.5^{\circ}$ E), following a fast-computing version proposed by Faggian et al. (2015).

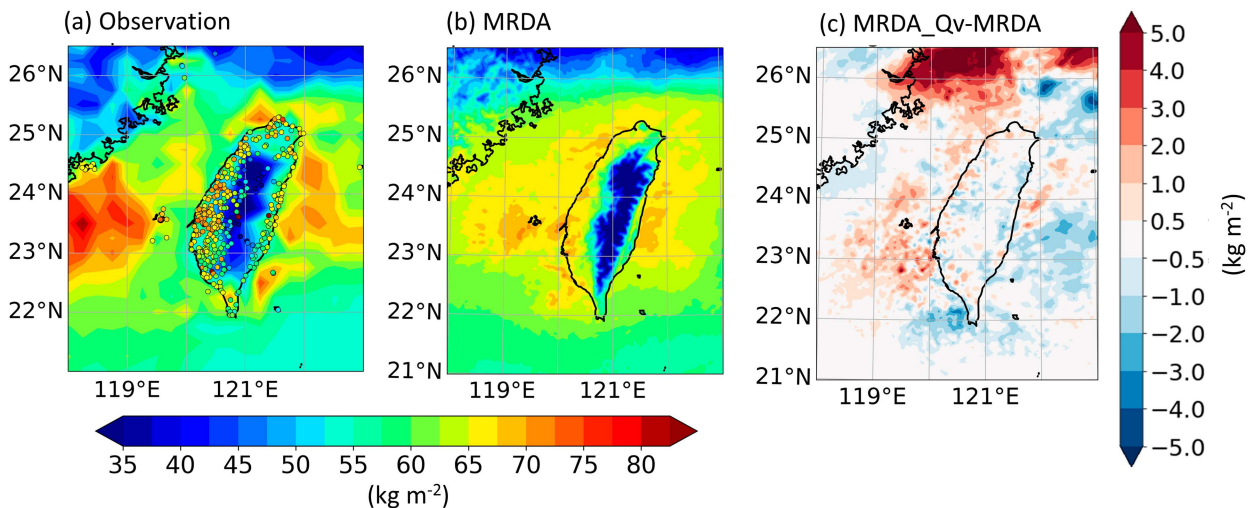


FIG. 18. TPW from (a) satellite (shading; mm) and (b) MRDA analysis at 0300 UTC 7 Jun. (c) The TPW difference between the MRDA\_Qv and MRDA analyses. The dots in (a) are the TPW derived from the ground-based Global Navigation Satellite System-ZTD.

FSS in Figs. 19a and 19b shows that MRDA, MRDA\_nSP, and MRDA\_Qv have better performance of rainfall forecasts. This is mainly attributed to the increase of the long-range moisture transport from upstream by assimilating Chigu

radar's radial velocity with the large localization during the first iteration in the SCL method. Therefore, using the SCL method in radar assimilation is critical for improving forecasting skills at all scales, which helps extend the radar's

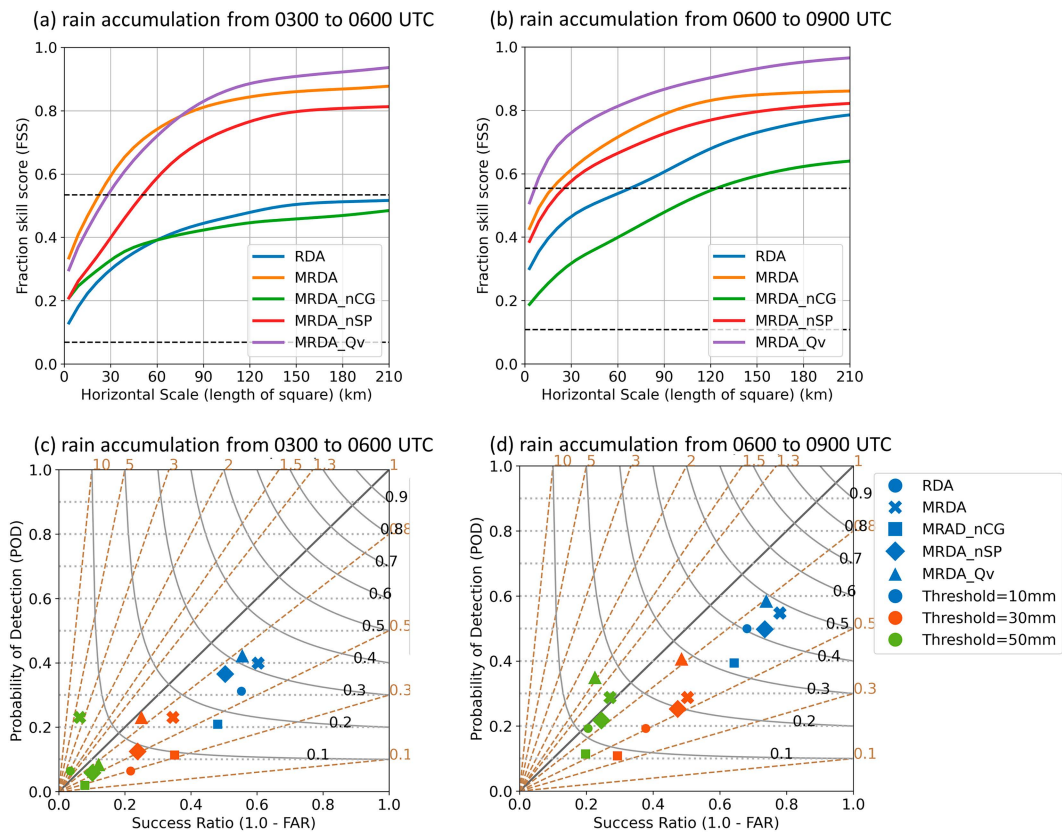


FIG. 19. FSSs of all the experiments for a 3-h rainfall accumulation from (a) 0300–0600 UTC and (b) 0600–0900 UTC 7 Jun. The lower and upper black dashed lines in (a) and (b) indicate the FSS for the random forecast and baseline of a skillful forecast, respectively. Performance diagrams for accumulated rainfall from (c) 0300 to 0600 UTC and (d) 0600 to 0900 UTC 7 Jun.

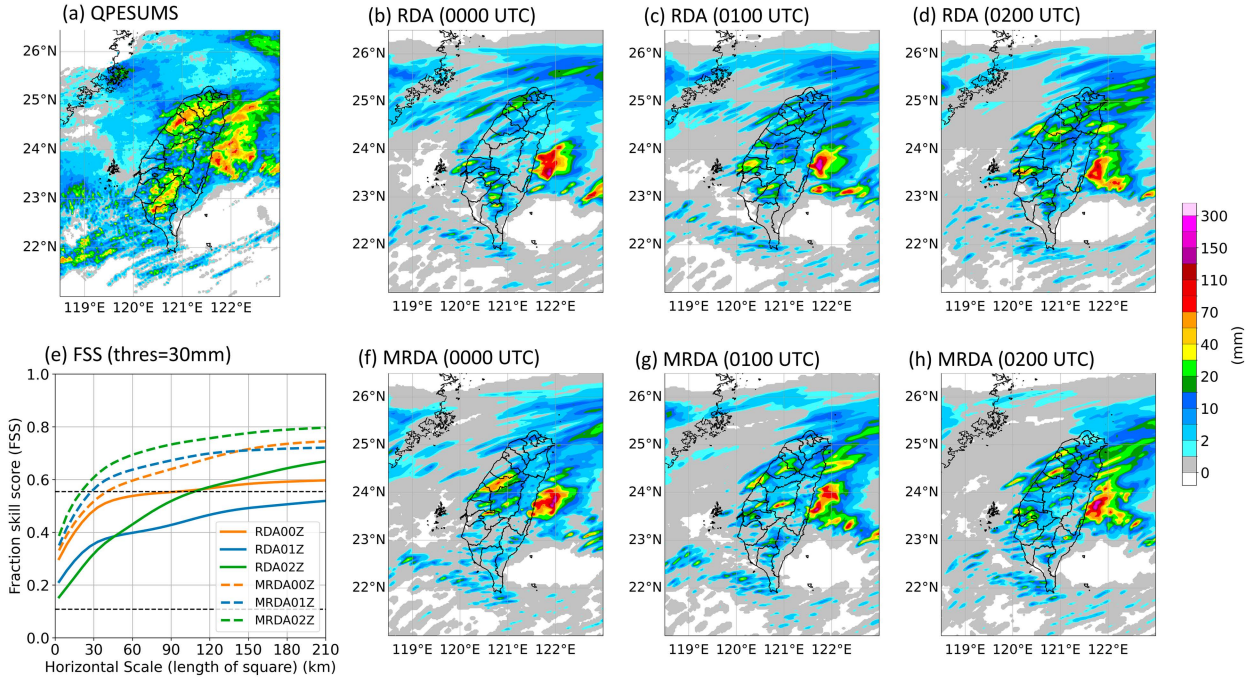


FIG. 20. Three-hourly accumulated rainfall from 0600 to 0900 UTC 7 Jun from (a) QPESUMS (repeating Fig. 7d here for easy comparison) and model forecasts from the RDA experiments, initialized by the ensemble analysis mean at (b) 0000 UTC, (c) 0100 UTC, and (d) 0200 UTC 7 Jun. (f)–(h) As in (b)–(d), but for MRDA. (e) The lower and upper black dashed lines indicate the FSS for the random forecast and baseline of a skillful forecast, respectively.

impact period in the forecast. Without long-range moisture transport from upstream, MRDA\_nCG becomes even less accurate than RDA for later forecasts. The assimilation of the S-Pol radar data affects convection intensification along the northwestern coast at the initial time and thus has a greater impact on the first 3-h forecast than on the second 3-h forecast. Although the moisture variable is not directly observed by radar and convective-scale localization for moisture is recommended, the use of multiscale moisture corrections allows MRDA\_Qv to have the highest FSS when a large verification area is used (i.e., the larger horizontal scale in Figs. 19a,b), particularly at later forecast hours.

Next, the performance diagrams, including the probability of detection (POD), success ratio, bias, and equitable threat score (ETS), are used to quantitatively evaluate the rainfall forecast skills from different experiments, as shown in Figs. 19c and 19d. In this diagram, the forecast skill is improved as the scores approach the diagonal line and is considered perfect as the scores move to the upper-right corner of the chart. The results show that the MRDA forecast is consistently more skillful than the RDA forecast at different rainfall thresholds. The advantage of using the SCL scheme is again even more evident at longer forecast hours. Because of the improvement in the forecast of the rainfall location, the MRDA POD is increased, and the false alarms are reduced. Owing to the increased rainfall amount, MRDA\_Qv further increases the POD for the forecast from 0600 to 0900 UTC. In contrast, MRDA\_nCG yields the

lowest scores because of the lack of moisture supply. It is also evident that the impact of S-Pol radar on the rainfall forecast skill is clearer during the early forecast (0300–0600 UTC).

#### b. Forecasts initialized at different times

Forecasts initialized at earlier times are examined to test the robustness of the better performance in MRDA than in RDA. Three additional pairs of deterministic forecasts of RDA and MRDA are conducted and initialized by ensemble mean analyses at 0000, 0100, and 0200 UTC 7 June. The results show that MRDA forecasts have robust performance and are more skillful than RDA forecasts are, particularly for longer forecast hours (0600–0900 UTC), as shown in the FSS (Fig. 20e). Compared with the RDA forecast (Figs. 20b–d), the MRDA forecasts can better predict heavy rain over western Taiwan, even when the forecast is initialized at 0000 UTC (Fig. 20b vs Fig. 20f). According to the FSS for precipitation prediction (Fig. 20e), the forecast skill of MRDA is comparable among the forecasts initialized at three successive hours, whereas the forecast skills vary substantially among the three RDA forecasts. Notably, the MRDA forecast has a higher score for smaller scales, reflecting its ability to better capture observed convective cell activity shown in Fig. 3.

#### 7. Summary and conclusions

This study investigates the mechanisms of the heavy rainfall event that occurred on Taiwan's western coast on 7 June 2022

during the IOP3 of the TAHOPE/PRECIP field campaign. Two numerical experiments were conducted, namely, MRDA and RDA, which differ in the assimilation of radial velocity via multiscale localizations and single convective-scale localization, respectively. The WRF-LETKF radar assimilation system (WLRAS) with 62 ensemble members is used for data assimilation cycling from 2100 UTC 6 June to 0300 UTC 7 June, with a rapid time interval of 12 min. The ensemble analysis mean at 0300 UTC 7 June is then used to initialize a 6-h deterministic forecast.

Compared with the RDA forecast, the MRDA forecast reveals heavy rainfall with locations and intensities that better resemble the observed patterns. In particular, the MRDA forecast demonstrates the advantage of using multiscale localizations (or the SCL method) for the later forecasting time, such as capturing the elongated rainband during the last three forecast hours from 0600 to 0900 UTC 7 June. Convective cells contributing to heavy coastal rainfall are better produced in the MRDA forecast, including the cell merging process. In comparison, the convection in the RDA forecast is less organized on the western coast.

The heavy rainfall on the western coast of Taiwan is attributed to convergence from the combined effects of a shallow mesovortex offshore of western central Taiwan and the frontal zone offshore of northwestern Taiwan. With the SCL method, the wind corrections can be derived in the data void region north of Penghu Island, which is critical for reshaping and relocating the shallow mesovortex toward western Taiwan. Compared with independent conventional observations in Penghu, southwest of Taiwan, the near-surface westerly winds in MRDA better match the observations than the southwesterly flow in RDA. The westerly wind component of the mesoscale vortex in MRDA greatly enhances convergence at the coast because of the friction difference between land and ocean and increases moisture transport and convective stability, supporting convection intensification at the coast of central Taiwan. The SCL method also provides a broader range of northerly wind corrections north of the frontal zone located northwest of Taiwan, and this, along with the easterly wind component south of the frontal zone (contributed by the mesoscale vortex), enhances the convergence and the temperature gradient in the frontal zone. As a result, line convection is well established in this region in MRDA. This strong convergence feature is critical for the rapid development of heavy coastal rainfall as line convection moves inland and merges with convection from the coast of central Taiwan.

Sensitivity experiments are conducted to examine the role of the Chigu and S-Pol radars and the use of the SCL method in water vapor corrections in heavy rainfall forecasts. Without the assimilation of Chigu radar data (MRDA\_nCG), reshaping and relocation of the mesovortex toward western Taiwan cannot be achieved. Consequently, the convergence and moisture transport due to the westerly component associated with the mesovortex and the rainfall in western central Taiwan were missed in the forecast. Without S-Pol radar (MRDA\_nSP), the mesoscale vortex was weaker, and the convergence at the frontal zone offshore of northwestern Taiwan disappeared, resulting in almost no rainfall occurring over northern

Taiwan. Last, the heavy rainfall in Taiwan can be further improved by applying multiscale corrections to moisture analysis (MRDA\_Qv); however, the moisture accuracy away from the area of interest can decrease because of sampling error, and thus, convective-scale localization is recommended.

Despite the good performance of the MRDA analysis and forecasting, multiscale corrections can be further improved. First, unlike the dual localization method, which derives the large-scale correction with the small-wavenumber component of the ensemble, in this study, the update with large localization uses the full resolution of the ensemble perturbations. This approach carries model information at all scales that cannot be disentangled during the first and second iterations of the SCL method. This may inevitably introduce sampling errors. However, such an issue does not overwhelm the positive impact of using the SCL method. This is because only subgroups of observations at lower horizontal densities are assimilated during the first two iterations. Methods that can separate the scales (e.g., that of [Sodhi and Fabry 2022](#)) may provide a better solution for correcting large-scale information.

**Acknowledgments.** Shu-Chih Yang is sponsored by the National Science Council Grants NSC-112-2111-M-008-015 and NSTC-112-2119-M-008-008. Shu-Hua Chen is partially supported by the U.S. National Science Foundation Award 1624414. The authors acknowledge TAHOPE, PRECIP, and CWA for the support and data collected during the field campaign and the service from Atmospheric Science Research and Application Databank (ASRAD) supported by Chinese Culture University and the National Science and Technology Council (NSTC 112-2740-M-001-007, NSTC 112-2740-M-034-001) of Taiwan.

**Data availability statement.** Radar data during the TAHOPE/PRECIP field campaign are available at the Atmospheric Science Research and Application Databank (ASRAD) ([https://exp.pccu.edu.tw:8142/annual\\_experiment/tahope2022/](https://exp.pccu.edu.tw:8142/annual_experiment/tahope2022/)). The satellite-derived total precipitable water data are from <https://bin.ssec.wisc.edu/pub/mtpw2/data/>. The radar and satellite datasets have some guaranteed lifetimes on the websites. The initial ensemble is from the NCEP global ensemble forecast available at <https://noaa-gefs-pds.s3.amazonaws.com/>. The WRF Model is publicly available at <https://github.com/wrf-model/WRF>. The WRF-LETKF radar assimilation system, analysis, and forecast data are available upon request.

## APPENDIX

### Quality Check of the Radar Data

To ensure the quality of the radar datasets, a rigorous quality control (QC) process was implemented in Taiwan's National Central University (NCU) Radar Laboratory's RAKIT (Radar kit) software. The main objective of this QC procedure was to eliminate nonmeteorological signals, such as ground clutter, and to correct velocity unfolding. For single-polarization radar (i.e., RCCG in this study), nonmeteorological signals originating from terrain and ground clutter in mountainous

areas are filtered out when  $Z_h$  exceeds 15 dBZ and  $V_r$  is less than  $2 \text{ m s}^{-1}$ , whereas signals near the radar are discarded when  $Z_h$  falls within the range from  $-50$  to  $20 \text{ dBZ}$  and when  $V_r$  is less than  $5 \text{ m s}^{-1}$ . For the dual-polarization radars (i.e., RCWF and S-Pol in this study), echoes with a correlation coefficient below a specified threshold (0.9 for RCWF and 0.85 for S-Pol) and a standard deviation of the differential phase ( $\phi_{DP}$ ) exceeding  $15^\circ$  for RCWF ( $10^\circ$  for S-Pol) are identified as nonmeteorological signals and are subsequently removed.

Unexpectedly, unwanted radiofrequency signals, characterized as dots, spokes, or stripes (see Fig. A1a for examples), are identified and treated as radiofrequency interference (RFI) (Saltikoff et al. 2016). These signals, potentially introduced by interfering radio local area networks (RLANs) for mobile services, pose a challenge to traditional QC procedures. To mitigate this issue, an additional algorithm is employed to target the gates meeting one of three criteria: First, gates with the azimuth angle  $\alpha$ , where the  $Z_h$  differs by more than  $15 \text{ dBZ}$  from neighboring beams at azimuth

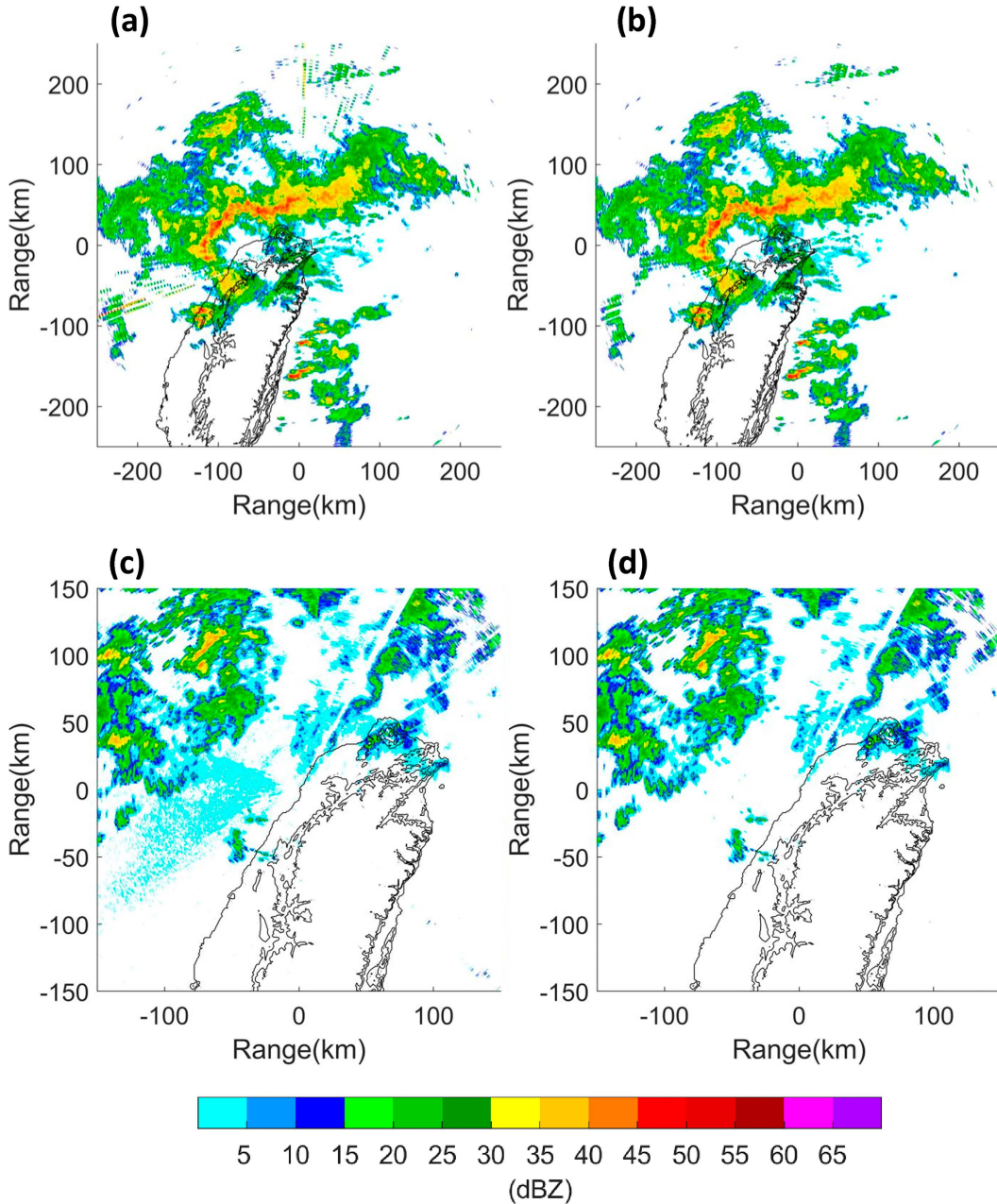


FIG. A1. Examples of radar reflectivity data (a) before and (b) after the RFI QC for the RCWF and (c) before and (d) after the removal of low reflectivity over the coastal ocean for the lowest elevation of the PPI ( $0.5^\circ$ ) for S-Pol.

$\alpha \pm 1$  at the same distance from the radar, are classified as spurious signals. These gates are removed if the proportion of identified gates along the same beam exceeds 25%. This procedure follows the concept of Ośrońska and Szturc (2022). Second, gates with differential reflectivity outside the range from  $-3$  to  $4$  dB are eliminated, following the approach of Yin et al. (2022). Finally, spurious signals are flagged when their phiDP values exceed  $200^\circ$  (the empirical value used in this study). This algorithm effectively mitigates RFI in the dataset used in this study (Fig. A1b as an example). Furthermore, eliminating uncertain data prone to spurious corrections in the wind and geopotential height fields is crucial during assimilation, particularly for multiscale corrections, as suggested by Liu (2022). Consequently, signals observed by S-Pol near the surface over coastal areas are removed when  $Z_h$  is smaller than  $-1$  dBZ and the signal-to-noise ratio for the same gate falls below a specified threshold of 0 (Fig. A1c vs Fig. A1d).

## REFERENCES

- Chang, P.-L., and Coauthors, 2021: An operational multi-radar multi-sensor QPE system in Taiwan. *Bull. Amer. Meteor. Soc.*, **102**, E555–E577, <https://doi.org/10.1175/BAMS-D-20-0043.1>.
- Chen, F., and J. Dudhia, 2001: Coupling an advanced land surface-hydrology model with the Penn State–NCAR MM5 modeling system. Part I: Model implementation and sensitivity. *Mon. Wea. Rev.*, **129**, 569–585, [https://doi.org/10.1175/1520-0493\(2001\)129<0569:CAALSH>2.0.CO;2](https://doi.org/10.1175/1520-0493(2001)129<0569:CAALSH>2.0.CO;2).
- Chen, G. T.-J., C.-C. Wang, and D. T.-W. Lin, 2005: Characteristics of low-level jets over northern Taiwan in mei-yu season and their relationship to heavy rain events. *Mon. Wea. Rev.*, **133**, 20–43, <https://doi.org/10.1175/MWR-2813.1>.
- Chen, Y.-L., Y.-J. Chu, C.-S. Chen, C.-C. Tu, J.-H. Teng, and P.-L. Lin, 2018: Analysis and simulations of a heavy rainfall event over northern Taiwan during 11–12 June 2012. *Mon. Wea. Rev.*, **146**, 2697–2715, <https://doi.org/10.1175/MWR-D-18-0001.1>.
- Chung, K.-S., W. Chang, L. Fillion, and M. Tanguay, 2013: Examination of situation-dependent background error covariances at the convective scale in the context of the ensemble Kalman filter. *Mon. Wea. Rev.*, **141**, 3369–3387, <https://doi.org/10.1175/MWR-D-12-00353.1>.
- Do, P.-N., K.-S. Chung, P.-L. Lin, C.-Y. Ke, and S. M. Ellis, 2022: Assimilating retrieved water vapor and radar data from NCAR S-PolKa: Performance and validation using real cases. *Mon. Wea. Rev.*, **150**, 1177–1199, <https://doi.org/10.1175/MWR-D-21-0292.1>.
- Faggian, N., B. Roux, P. Steinle, and B. Ebert, 2015: Fast calculation of the fractions skill score. *Mausam*, **66**, 457–466, <https://doi.org/10.54302/mausam.v66i3.555>.
- Hong, S.-Y., Y. Noh, and J. Dudhia, 2006: A new vertical diffusion package with an explicit treatment of entrainment processes. *Mon. Wea. Rev.*, **134**, 2318–2341, <https://doi.org/10.1175/MWR3199.1>.
- Hsiao, F., and Y.-L. Chen, 2014: Revisiting the structure and characteristics of an early summer monsoon trough over South China in 1975. *SOLA*, **10**, 194–198, <https://doi.org/10.2151/sola.2014-041>.
- Hunt, B. R., E. J. Kostelich, and I. Szunyogh, 2007: Efficient data assimilation for spatiotemporal chaos: A local ensemble transform Kalman filter. *Physica D*, **230**, 112–126, <https://doi.org/10.1016/j.physd.2006.11.008>.
- Iacono, M. J., J. S. Delamere, E. J. Mlawer, M. W. Shephard, S. A. Clough, and W. D. Collins, 2008: Radiative forcing by long-lived greenhouse gases: Calculations with the AER radiative transfer models. *J. Geophys. Res.*, **113**, D13103, <https://doi.org/10.1029/2008JD009944>.
- Jou, B. J.-D., W.-C. Lee, and R. H. Johnson, 2011: An overview of SoWMEX/TiMREX. *The Global Monsoon System*, B. Wang et al., Eds., World Scientific Publishing Company, 303–318.
- Kain, J. S., 2004: The Kain–Fritsch convective parameterization: An update. *J. Appl. Meteor.*, **43**, 170–181, [https://doi.org/10.1175/1520-0450\(2004\)043<0170:TKCPAU>2.0.CO;2](https://doi.org/10.1175/1520-0450(2004)043<0170:TKCPAU>2.0.CO;2).
- Ke, C.-Y., K.-S. Chung, T.-C. Chen Wang, and Y.-C. Liou, 2019: Analysis of heavy rainfall and barrier-jet evolution during Mei-Yu season using multiple Doppler radar retrievals: A case study on 11 June 2012. *Tellus*, **71A**, 1571369, <https://doi.org/10.1080/16000870.2019.1571369>.
- Kuo, Y.-H., and G. T.-J. Chen, 1990: The Taiwan Area Mesoscale Experiment (TAMEX): An overview. *Bull. Amer. Meteor. Soc.*, **71**, 488–503, [https://doi.org/10.1175/1520-0477\(1990\)071<0488:TTAMEA>2.0.CO;2](https://doi.org/10.1175/1520-0477(1990)071<0488:TTAMEA>2.0.CO;2).
- Lin, G.-W., and H. Chen, 2012: The relationship of rainfall energy with landslides and sediment delivery. *Eng. Geol.*, **125**, 108–118, <https://doi.org/10.1016/j.enggeo.2011.11.010>.
- Lin, K., S. Yang, and S. S. Chen, 2022: Improving analysis and prediction of tropical cyclones by assimilating radar and GNSS-R wind observations: Ensemble data assimilation and observing system simulation experiments using a coupled atmosphere–ocean model. *Wea. Forecasting*, **37**, 1533–1552, <https://doi.org/10.1175/WAF-D-21-0202.1>.
- Liu, J.-Y., 2022: Analyzing the convection development over northern Taiwan using a multi-scale radar data assimilation system with rapid update cycles. M.S. Thesis, Dept. of Atmospheric Science, National Central University, 126 pp.
- Luo, Y., and Y. Chen, 2015: Investigation of the predictability and physical mechanisms of an extreme-rainfall-producing mesoscale convective system along the Meiyu front in East China: An ensemble approach. *J. Geophys. Res. Atmos.*, **120**, 10 593–10 618, <https://doi.org/10.1002/2015JD023584>.
- Miyoshi, T., and K. Kondo, 2013: A multi-scale localization approach to an ensemble Kalman filter. *SOLA*, **9**, 170–173, <https://doi.org/10.2151/sola.2013-038>.
- Ośrońska, K., and J. Szturc, 2022: Improvement in algorithms for quality control of weather radar data (RADVOL-QC system). *Atmos. Meas. Tech.*, **15**, 261–277, <https://doi.org/10.5194/amt-15-261-2022>.
- Roberts, N. M., and H. W. Lean, 2008: Scale-selective verification of rainfall accumulations from high-resolution forecasts of convective events. *Mon. Wea. Rev.*, **136**, 78–97, <https://doi.org/10.1175/2007MWR2123.1>.
- Saltikoff, E., J. Y. N. Cho, P. Tristant, A. Huuskonen, L. Allmon, R. Cook, E. Becker, and P. Joe, 2016: The threat to weather radars by wireless technology. *Bull. Amer. Meteor. Soc.*, **97**, 1159–1167, <https://doi.org/10.1175/BAMS-D-15-00048.1>.
- Skamarock, W. C., and Coauthors, 2019: A description of the Advanced Research WRF Model version 4.1. NCAR Tech. Note NCAR/TN-556+STR, 162 pp., <https://doi.org/10.5065/1dfh-6p97>.
- Sodhi, J. S., and F. Fabry, 2022: Benefits of smoothing backgrounds and radar reflectivity observations for multiscale data assimilation with an ensemble Kalman filter at convective

- scales: A proof-of-concept study. *Mon. Wea. Rev.*, **150**, 589–601, <https://doi.org/10.1175/MWR-D-21-0130.1>.
- Tao, W.-K., J. Simpson, and M. McCumber, 1989: An ice-water saturation adjustment. *Mon. Wea. Rev.*, **117**, 231–235, [https://doi.org/10.1175/1520-0493\(1989\)117<0231:AIWSA>2.0.CO;2](https://doi.org/10.1175/1520-0493(1989)117<0231:AIWSA>2.0.CO;2).
- Tsai, C.-C., S.-C. Yang, and Y.-C. Liou, 2014: Improving quantitative precipitation nowcasting with a local ensemble transform Kalman filter radar data assimilation system: Observing system simulation experiments. *Tellus*, **66A**, 21804, <https://doi.org/10.3402/tellusa.v66.21804>.
- Tu, C.-C., Y.-L. Chen, P.-L. Lin, and M.-Q. Huang, 2022: Analysis and simulations of a heavy rainfall event associated with the passage of a shallow front over northern Taiwan on 2 June 2017. *Mon. Wea. Rev.*, **150**, 505–528, <https://doi.org/10.1175/MWR-D-21-0113.1>.
- Wang, X., H. G. Chipilski, C. H. Bishop, E. Satterfield, N. Baker, and J. S. Whitaker, 2021: A multiscale local gain form ensemble transform Kalman filter (MLGETKF). *Mon. Wea. Rev.*, **149**, 605–622, <https://doi.org/10.1175/MWR-D-20-0290.1>.
- Wu, P.-Y., S.-C. Yang, C.-C. Tsai, and H.-W. Cheng, 2020: Convective-scale sampling error and its impact on the ensemble radar data assimilation system: A case study of a heavy rainfall event on 16 June 2008 in Taiwan. *Mon. Wea. Rev.*, **148**, 3631–3652, <https://doi.org/10.1175/MWR-D-19-0319.1>.
- Yang, S.-C., S.-H. Chen, K. Kondo, T. Miyoshi, Y.-C. Liou, Y.-L. Teng, and H.-L. Chang, 2017: Multilocalization data assimilation for predicting heavy precipitation associated with a multiscale weather system. *J. Adv. Model. Earth Syst.*, **9**, 1684–1702, <https://doi.org/10.1002/2017MS001009>.
- , Z.-M. Huang, C.-Y. Huang, C.-C. Tsai, and T.-K. Yeh, 2020: A case study on the impact of ensemble data assimilation with GNSS zenith total delay and radar data on heavy rainfall prediction. *Mon. Wea. Rev.*, **148**, 1075–1098, <https://doi.org/10.1175/MWR-D-18-0418.1>.
- , H.-W. Cheng, P.-Y. Wu, Z.-M. Huang, and C.-C. Tsai, 2022: Convective-scale data assimilation and precipitation prediction with a local ensemble transform Kalman filter radar assimilation system over complex terrain: A thorough investigation with the heavy rainfall in Taiwan on 16 June 2008. *Data Assimilation for Atmospheric, Oceanic and Hydrologic Applications (Vol. IV)*, S. K. Park and L. Xu, Eds., Springer, 543–579.
- Yeh, H.-L., S.-C. Yang, K. Terasaki, T. Miyoshi, and Y.-C. Liou, 2022: Including observation error correlation for ensemble radar radial wind assimilation and its impact on heavy rainfall prediction. *Quart. J. Roy. Meteor. Soc.*, **148**, 2254–2281, <https://doi.org/10.1002/qj.4302>.
- Yeh, T.-K., J.-S. Hong, C.-S. Wang, C.-H. Chen, K.-H. Chen, and C.-T. Fong, 2016: Determining the precipitable water vapor with ground-based GPS and comparing its yearly variation to rainfall over Taiwan. *Adv. Space Res.*, **57**, 2496–2507, <https://doi.org/10.1016/j.asr.2016.04.002>.
- Yin, J., P. Hoogeboom, C. Unal, and H. Russchenberg, 2022: Radio frequency interference characterization and mitigation for polarimetric weather radar: A study case. *IEEE Trans. Geosci. Remote Sens.*, **60**, 5102616, <https://doi.org/10.1109/TGRS.2021.3093565>.
- Zhang, F., Y. Weng, J. A. Sippel, Z. Meng, and C. H. Bishop, 2009: Cloud-resolving hurricane initialization and prediction through assimilation of Doppler radar observations with an ensemble Kalman filter. *Mon. Wea. Rev.*, **137**, 2105–2125, <https://doi.org/10.1175/2009MWR2645.1>.
- Zhang, Y., X. Chen, and M. M. Bell, 2023: Improving short-term QPF using geostationary satellite all-sky infrared radiances: Real-time ensemble data assimilation and forecast during the PRECIP 2020 and 2021 experiments. *Wea. Forecasting*, **38**, 591–609, <https://doi.org/10.1175/WAF-D-22-0156.1>.